Journal of Sound and Vibration 618 (2025) 119293

Contents lists available at ScienceDirect

Journal of Sound and Vibration

journal homepage: www.elsevier.com/locate/jsvi

The Advection Boundary Law in presence of mean flow and plane wave excitation: Passivity, nonreciprocity and enhanced noise transmission attenuation

E. De Bono [a],*, M. Collet [a], M. Ouisse [b], E. Salze [c], M. Volery [d], H. Lissek [d], J. Mardjono [e]

[a] Ecole Centrale de Lyon, CNRS, ENTPE, LTDS, UMR5513, 69130 Ecully, France
[b] SUPMICROTECH, Université de Franche-Comté, CNRS, institut FEMTO-ST, F-25000 Besançon, France
[c] Univ. Lyon, École Centrale de Lyon, LMFA UMR 5509, F-69134 Ecully, France
[d] Signal Processing Laboratory LTS2, Ecole Polytechnique Fédérale de Lausanne, Station 11, CH-1015, Lausanne, Switzerland
[e] Safran Aircraft Engines, F-75015, Paris, France

ARTICLE INFO

Keywords:
Acoustic liners
Impedance control
Nonreciprocal propagation
Active noise control
Programmable boundary
Generalized impedance

ABSTRACT

This paper follows a previous publication, where the so-called Advection Boundary Law lining an acoustic waveguide, in absence of mean flow, was studied in terms of its potentials for noise isolation and non-reciprocal propagation. The Advection Boundary Law is a special operator which can be synthesized on the boundary of a waveguide thanks to a programmable Electroacoustic Liner. This special boundary operator proved to achieve enhanced noise isolation with respect to classical local impedance. Moreover, it demonstrated to accomplish non-reciprocal sound propagation along the waveguide, and the non-trivial passivity limits were assessed. Nevertheless, acoustic liners are meant to attenuate noise propagation in waveguides with airflow, such as heating and air-conditioning ventilation systems and aircraft turbofan engines. In particular, the new generation of Ultra-High-By-Pass-Ratio turbofans and the increasingly stringent regulations on aircraft noise pollution, require a significant breakthrough in the acoustic liner technology. This challenge was taken up by the SALUTE H2020 project, during which the experimental campaign reported in this paper was conducted. For the first time, the Advection Boundary Law interfacing an airflow is thoroughly analysed in terms of duct-modes and scattering simulations. The enhancement of isolation performances is confirmed also in presence of mean-flow. Moreover, for the first time, non-reciprocal propagation along the waveguide is achieved against the one naturally induced by the mean-flow. These results, along with the passivity limits, are discussed and confirmed by the experimental campaign, conducted on the CAIMAN test-bench of the Laboratory of Fluid Mechanics and Acoustics of the Ecole Centrale de Lyon. The tools and results provided in this paper should lead the implementation of the Advection Boundary Law for maximizing noise isolation or achieving non-reciprocal sound propagation along waveguides with airflow.

1. Introduction

The noise transmission mitigation in waveguides by parietal acoustic treatment interests several industrial fields, like heating and air-conditioning ventilation systems and aircraft turbofan engines. Its main challenge is the need to provide noise attenuation along

* Corresponding author.
E-mail address: emanueledeb88@hotmail.it (E. De Bono).

https://doi.org/10.1016/j.jsv.2025.119293
Received 23 February 2025; Received in revised form 26 May 2025; Accepted 10 June 2025

Available online 21 June 2025

the direction which is parallel to the surface where acoustic liner is applied (so called ‘‘grazing-incidence problem’’). This is necessary as the liner should have minimal impact on the aerodynamic flow going through the duct. The sufficient condition for the boundary to fully control the wave propagation in an acoustic domain is that every ray of the acoustic field interacts with the boundary [1]. Therefore, the solution to the full controllability problem of sound waves in the grazing incidence case is, mathematically speaking, unsolvable, but optimal *impedances* minimizing the transmitted sound can be looked for. The Cremer's optimal impedances [2–4] are analytical solutions to the problem of maximizing the attenuation of specific duct-modes in an infinite waveguide. This problem is formulated in the frequency domain, and indeed, unfortunately, leads to *non-real* impedance operators, in the sense that their inverse Fourier transform does not produce a real function in the time domain (the *reality* condition [5] is unfulfilled). Therefore, the Cremer impedance can only be achieved at discrete frequencies [6,7]. Moreover, the *optimality* of Cremer's impedance quickly weakens as the finite dimension of the liner is taken into account, and airflow becomes significant [4,8]. Meanwhile, from the seminal work of [9], the impedance control strategy has opened the doors towards boundary behaviours more sophisticated than locally reacting impedances. In [10–12], a *generalized impedance* has been studied, involving the spatial derivative of sound pressure: the so-called Advection Boundary Law (ABL). This has been the first step towards the study of non-local boundary operators (in time or in space [13]), and their potentials to overcome the classical local impedance behaviour to optimize noise isolation in grazing incidence. In particular, in [12], the physical interpretation of the ABL has been provided thanks to Dirichlet-to-Neumann (DtN) mapping [14], and a thorough numerical and experimental investigation demonstrated its potential to enhance noise isolation with respect to locally-reacting impedances of resonators and to achieve important non-reciprocal acoustic propagation (a highly desirable feature for many physical domains and applications [15]). The technology allowing to implement the ABL is the so-called Electroacoustic Liner (EL). The EL is made of an array of programmable Electroacoustic Resonators (ERs), each one composed of 4 microphones (to retrieve the average sound pressure and its first spatial derivative) and a loudspeaker. Based upon the estimated pressure and its spatial derivative, the ABL generalized impedance operator is implemented by piloting the loudspeaker membrane velocity, driven by the controlled electrical current in the speaker coil. The control algorithm is designed by model-inversion [16], based upon the estimated mechanical dynamics of the loudspeaker, and has been recently extended to contemplate also nonlinear target dynamics at low excitation levels [17–21]. Such control architecture, first devised in [22], demonstrated its efficiency for both room-modes damping [22,23] and sound transmission mitigation in waveguides [24–35], despite the effect of time delay in the digital control, affecting the acoustical passivity margins [36]. Nevertheless, so far, the specific effect of the presence of an airflow upon the ABL, has never been fully investigated. Moreover, in order to protect the electroacoustic devices from the flow, the EL needs a layer, composed of a perforated plate and a wiremesh, allowing to separate, to a certain extent, the aerodynamics (in the duct) from the acoustics (on the EL). In Section 3, the duct mode analysis is conducted to preliminary assess the performances of the ABL lining an infinite waveguide, with airflow up to Mach 0.3. Then, in Section 4, the scattering performances of the ABL are simulated in a 2D waveguide. Then, the experimental validation is discussed in Section 5. Finally, in Section 6, a summary of the results is provided, along with the envisaged future developments. In each step of the present work, the impact of airflow upon the ABL acoustical passivity and performances, both in terms of noise isolation and non-reciprocal propagation, is highlighted. The enhancement of noise isolation with respect to local impedance resonators, is confirmed also in presence of airflow. Moreover, here, for the first time and contrary to previous works [37,38], the airflow is not exploited to *induce* the non-reciprocal propagation. Indeed, the non-reciprocity generated by the ABL, can either be reinforced or opposed by the presence of flow, depending upon the airflow direction: if the flow has the same direction as the synthetic boundary advection in the ABL, then the non-reciprocity is enhanced, while in case air is flowing in the opposite direction of the synthetic boundary advection speed, the non-reciprocity is weakened. In this paper, we also demonstrate, both numerically and experimentally, the unique achievement of the ABL in counteracting, and even reversing, the non-reciprocity naturally induced by the airflow.

To resume, the significance and novelty of the ABL stays in the possibility to enhance the attenuation of noise transmission with respect to classical local impedance approaches, also in presence of mean-flow. Moreover, the ABL achieves unprecedented non-reciprocal propagation features despite the presence of flow.

2. Advection boundary law in open field

The theoretical conception of the ABL and its physical interpretation are already discussed in [12]. The generalized impedance Partial-Differential-Equation (PDE) of the ABL, writes:

$$Z_{\text{Loc}}(\partial_t) * \partial_t^2 u_n = \partial_t p + U_b \partial_x p \quad \text{on } \partial\Omega, \tag{1}$$

where $Z_{\text{Loc}}(\partial_t)$ is a general local impedance operator, $*$ is the convolution operation, u_n is the outward normal displacement on the boundary $\partial\Omega$, p is the sound pressure, U_b is the synthetic advection speed, while ∂_t is the Eulerien first time derivative and ∂_x is the x-derivative, with x a tangential coordinate on $\partial\Omega$. In particular, $Z_{\text{Loc}}(\partial_t)$ is here considered as a single-degree-of-freedom (SDOF) resonator impedance. Notice that the synthetic advection speed U_b represents an artificial convection which can be synthesized by the EL. Indeed, from [12], we know that Eq. (1) is the DtN mapping [14] of a semi-infinite propagative domain Ω_{fict}, on the interface $\partial\Omega$ with the actual air domain Ω_{air}. Such Ω_{fict} is characterized by a convection speed U_b along x. Therefore, the ABL mimics the interface with an advected domain behind the surface where the ABL is applied. From this, it comes the label of ABL and the meaning of synthetic advection. Notice that such U_b is not related to the grazing flow speed possibly present in the duct. The objective of this paper is, indeed, to verify the effect of a grazing flow over the performances of the ABL, i.e. to study the case of simultaneous presence of a synthetic boundary advection U_b, and the convection induced by grazing air flow.

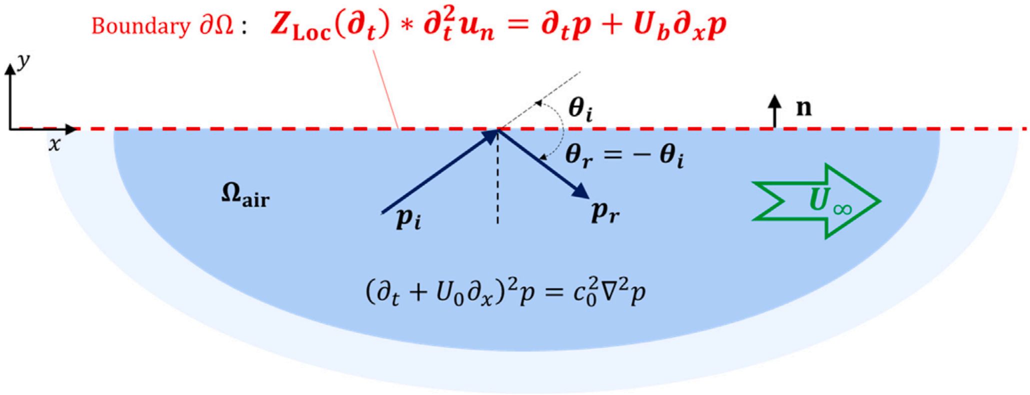

Fig. 1. ABL interfacing a semi-infinite domain with longitudinal airflow.

Notice that in Eq. (1), we preferred to express the ABL in terms of the normal displacement u_n, rather than in terms of the normal velocity v_n (which was employed in [12]). This is so, because now we are interested in the ABL effect upon an Ω_{air} traversed by an inviscid and irrotational mean-flow along x of velocity U_∞ and subsonic Mach $M_\infty = U_\infty/c_0$, with c_0 the sound speed. Indeed, for an acoustic domain with tangential flow, according to Ingard-Myers [5,39,40], the continuity of normal velocity is replaced by the continuity of normal displacement at the interface $\partial\Omega$ as appropriate boundary condition (BC).

Observe that the ABL refers to a BC, which is artificially synthesized by the EL, and which is physically targeted at the interface between each ER and the air. On the other hand, the Ingard-Myers [5,39,40] BC is a simplified way to numerically model the effect of the boundary layer due to the presence of mean-flow, with all its limitations [8].

As in [12], our first 2D case study is the ABL interfacing a semi-infinite air domain $\Omega_{\mathrm{air}} = [-\infty, \infty] \times [-\infty, 0]$, this time traversed by a tangential flow U_∞, as showed in Fig. 1. The treated boundary $\partial\Omega$ extends on all the x axis.

A general time-harmonic (in the usual complex notation $\mathrm{j}\omega t$) wave propagating in the semi-infinite domain Ω_{air} at an angle θ with respect to the x axis, has the form:

$$\bar{p}_w(t,\omega,x,y) = p_0(\omega) e^{\mathrm{j}\omega t - \mathrm{j}k_x x - \mathrm{j}k_y y}, \tag{2}$$

where $\bar{p}_w$ is the complex representation of $p_w = \mathrm{Re}\{\bar{p}_w\}$ and represents a general wave propagating in Ω_{air}, while k_x and k_y are the x and y components of the wavenumber vector. By replacing Eq. (2), in the convected wave equation $D_t^2 p = c_0^2 \nabla^2 p$, where $D_t = \partial_t + U_\infty \partial_x$ is the Lagrangian (also called convected) time derivative, we obtain:

$$k_x = \frac{k_0 \cos\theta}{1 + M_\infty \cos\theta}, \tag{3a}$$

$$k_y = \frac{k_0 \sin\theta}{1 + M_\infty \cos\theta}, \tag{3b}$$

where $k_0 = \omega/c_0$. We can now compute the reflection coefficient of the ABL in open-field with mean flow, starting from the definition of the incident time-harmonic sound field:

$$\bar{p}_i(t,\omega,x,y) = p_{i0}(\omega) e^{\mathrm{j}\omega t - \mathrm{j}k_x x - \mathrm{j}k_y y}, \tag{4}$$

where $\bar{p}_i$ is the complex representation of $p_i = \mathrm{Re}\{\bar{p}_i\}$, k_x and k_y are given by Eqs. (3a) and (3b) respectively, with $\theta = \theta_i$ the incident angle of the plane wave on the boundary $\partial\Omega$. The reflected wave field is supposed to respect the classical Snell–Descartes law of refraction, according to which the reflected plane wave propagates with a specular angle with respect to the incident one, i.e. $\theta_r = -\theta_i$. Hence, the complex reflected wave from an ABL can be written as:

$$\bar{p}_r(t,\omega,x,y) = R(\omega,\theta_i) p_{i0} e^{\mathrm{j}\omega t - \mathrm{j}k_x x + \mathrm{j}k_y y}, \tag{5}$$

with R the reflection coefficient at the oblique incidence θ_i.

In Eq. (6), the Euler equation of acoustics is projected along y, on the boundary $\partial\Omega$: $y = 0$.

$$-\rho_0 \left(\mathrm{j}\omega + U_\infty \partial_x\right)^2 \bar{u}_y(t,\omega,x) = \partial_y \bar{p}(t,\omega,x). \tag{6}$$

The displacement $\bar{u}_y$ on $\partial\Omega$ is obtained by the ABL of Eq. (1) as:

$$\bar{u}_y(t,\omega,x) = \frac{Y_{\mathrm{Loc}}(\mathrm{j}\omega)}{(\mathrm{j}\omega)^2} \left(\mathrm{j}\omega + U_b \partial_x\right) \bar{p}(t,\omega,x), \tag{7}$$

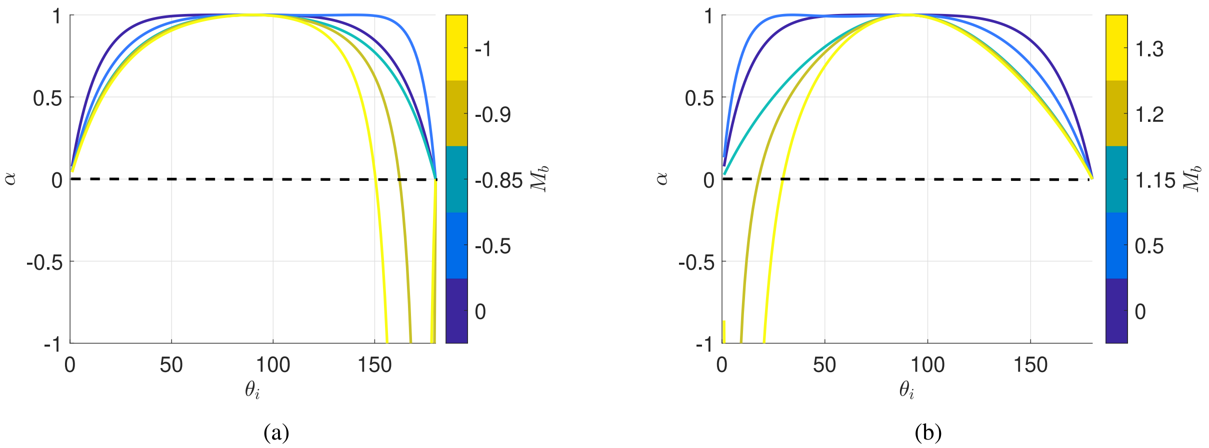

Fig. 2. ABL absorption coefficient versus θ_i, in open field, for $M_\infty = 0.15$, $\eta_{\text{Loc}} = 1$ and varying $M_b \le 0$ (a) or $M_b \ge 0$ (b).

where $Y_{\text{Loc}} = 1/Z_{\text{Loc}}$ and $\bar{p} = \bar{p}_i + \bar{p}_r$. By replacing Eq. (7) in Eq. (6), we get:

$$\partial_y \bar{p}(t,\omega,x) = -\rho_0 \left(\mathrm{j}\omega + U_\infty \partial_x\right)^2 \frac{Y_{\text{Loc}}(\mathrm{j}\omega)}{(\mathrm{j}\omega)^2} \left(\mathrm{j}\omega + U_b \partial_x\right) \bar{p}(t,\omega,x). \tag{8}$$

Replacing Eqs. (4) and (5), in $\bar{p} = \bar{p}_i + \bar{p}_r$, after some algebraic computation, we obtain:

$$R(\omega,\theta_i) = \frac{1 - \frac{\eta_{\text{eff}}(\mathrm{j}\omega)}{\sin\theta_i(1+M_\infty\cos\theta_i)}}{1 + \frac{\eta_{\text{eff}}(\mathrm{j}\omega)}{\sin\theta_i(1+M_\infty\cos\theta_i)}}, \tag{9}$$

where η_{eff} is defined as:

$$\eta_{\text{eff}}(\mathrm{j}\omega, M_b, M_\infty, \theta_i) = \eta_{\text{Loc}}(\mathrm{j}\omega)\left(1 - \frac{M_b\cos\theta_i}{1 + M_\infty\cos\theta_i}\right), \tag{10}$$

where $M_b = U_b/c_0$ and $\eta_{\text{Loc}}(\mathrm{j}\omega) = \rho_0 c_0 Y_{\text{Loc}}(\mathrm{j}\omega)$. Observe that Eq. (9) is equivalent to the reflection coefficient obtained in [39] with a local normalized mobility coincident with the η_{eff} of Eq. (10). Observe also that, for $M_\infty = 0$, Eq. (9) retrieves the reflection coefficient reported in [12] in absence of mean flow. Notice that η_{eff} depends also on M_∞, M_b and θ_i. In particular, it is interesting to remark that for $M_b = -1 + M_\infty$, if $\theta_i \to 0$ then $\eta_{\text{eff}} \to 2\eta_{\text{Loc}}$, whereas if $\theta_i \to \pi$ then $\eta_{\text{eff}} \to 0$. Vice versa, for $M_b = 1 + M_\infty$, if $\theta_i \to 0$ then $\eta_{\text{eff}} \to 0$, whereas if $\theta_i \to \pi$ then $\eta_{\text{eff}} \to 2\eta_{\text{Loc}}$. This result preliminarily demonstrates the non-reciprocal propagation in grazing incidence that the ABL can achieve *in presence of mean-flow*, as detailed in the next sections.

Based on η_{eff}, we can write the absorption coefficient:

$$\alpha(\omega,\theta_i,M_\infty,M_b) = \frac{4\,\frac{\mathrm{Re}\{\eta_{\text{eff}}(\mathrm{j}\omega,\theta_i,M_\infty,M_b)\}}{\sin\theta_i(1+M_\infty\cos\theta_i)}}{1 + \left|\frac{\eta_{\text{eff}}(\mathrm{j}\omega,\theta_i,M_\infty,M_b)}{\sin\theta_i(1+M_\infty\cos\theta_i)}\right|^2} \tag{11}$$

From Eq. (11), we can apply the classical passivity condition for locally-reacting boundaries [5] to $\eta_{\text{eff}}(\mathrm{j}\omega,\theta_i M_\infty, M_b)$:

$$\mathrm{Re}\left\{\eta_{\text{eff}}(\mathrm{j}\omega,\theta_i,M_b)\right\} \ge 0 \quad \text{i.e.} \quad \mathrm{Re}\left\{\eta_{\text{Loc}}(\mathrm{j}\omega)\right\}\left(1 - \frac{M_b\cos\theta_i}{1+M_\infty\cos\theta_i}\right) \ge 0. \tag{12}$$

Eq. (12) is valid for any $\theta_i \in (0,\pi)$, as long as $\mathrm{Re}\{\eta_{\text{Loc}}(\mathrm{j}\omega)\} \ge 0$ (the local impedance operator should be passive) and $-1 + M_\infty \le M_b \le 1/1 + M_\infty$.

The ABL absorption coefficient versus the angle of incidence is plotted in Fig. 2 for $M_\infty = 0.15$, $\eta_{\text{Loc}} = 1$ and different values of M_b. Notice that the passivity condition on M_b reported above assures a positive α at any angle of incidence, while moving away from the passivity region brings about a larger range of angles of incidence θ_i for which $\alpha < 0$. Moreover, for $M_b < -1 + M_\infty$, the loss of acoustical passivity happens only for $\pi/2 < \theta_i < \pi$ (see Fig. 2(a)), while for $M_b > 1 + M_\infty$, the passivity loss happens only for $0 < \theta_i < \pi/2$. This means that the ABL can become non-passive only for waves propagating with $\mathrm{sgn}(k_x) = \mathrm{sgn}(M_b)$. As mentioned in [12], the dependence upon the angle of incidence of ABL acoustical passivity is a unique feature of the ABL with respect to classical liners, also in case of mean-flow. This angle-of-incidence dependency of ABL acoustical passivity manifests in a duct-mode dependent stability, which is analysed the next section.

3. Duct modes analysis in 2D waveguide

After having defined the passivity condition of the ABL on a semi-infinite domain, let us investigate the passivity and attenuation performances into an acoustic waveguide with mean flow, starting from the duct mode analysis. The general formulation of the

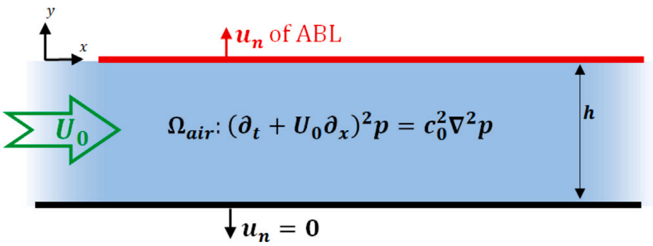

Fig. 3. Sketch of the 2D infinite waveguide with airflow, and upper side lined by the ABL.

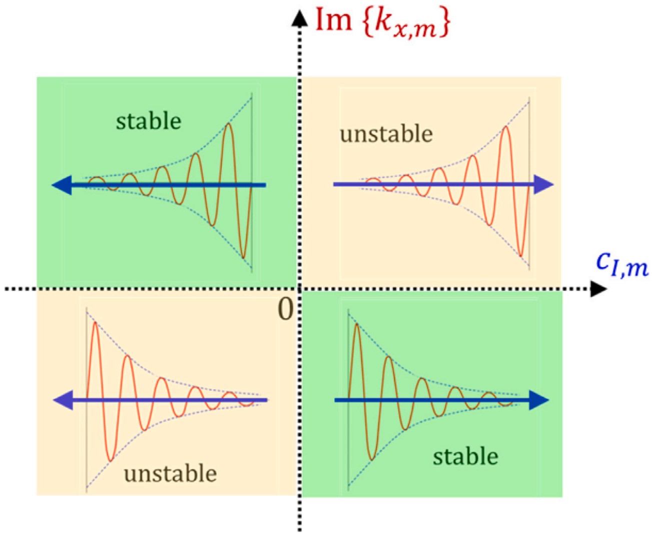

Fig. 4. Stability regions of duct-modes in the ($c_{E,m}$, Im$\{k_{x,m}\}$)-plane.

duct-mode eigen-problem in presence of mean flow is provided in Appendix A, and is solved by Finite Elements (FEs). The FE mesh has been built sufficiently fine to have large number of elements in the cross section and accurately resolve for each duct-mode shape of interest. We consider a 2D duct of section width $h = 0.111$ m, with only the upper wall lined by the ABL, as in Fig. 3. According to the assumption of duct mode eigen-solution:

$$\bar{p}_m(t, \omega, x, y) = A_m \psi_m(y, \omega) e^{j\omega t - jk_{x,m}(\omega)x}, \tag{13}$$

the duct mode analysis consists in computing the duct-mode eigenvalues ($k_{x,m}$) and eigenvectors (ψ_m), while A_m can be normalized at will. The duct-mode representation of the acoustic field, gives the occasion to define the average *modal acoustic intensity* $I_{x,m}$ along x and the *modal overall acoustic energy* $E_{\mathrm{tot},m}$. From the conservation of acoustic energy in case of irrotational and isentropic flow [5,41,42], the energy propagation speed along x of mode m [41,42] can be defined as the ratio between $I_{x,m}$ and $E_{\mathrm{tot},m}$. From [5,40], the *local* modal acoustic intensity vector writes:

$$\mathbf{I}_m(\omega, x, y) = \frac{1}{2}\mathrm{Re}\left\{ \left(\bar{p}_m(\omega, x, y) + \mathbf{M}_\infty \cdot \bar{\mathbf{v}}_m(\omega, x, y)\rho_0 c_0 \right)^* \left(\bar{\mathbf{v}}_m(\omega, x, y) + \mathbf{M}_\infty \frac{\bar{p}_m(\omega, x, y)}{\rho_0 c_0} \right) \right\}, \tag{14}$$

where $\bar{\mathbf{v}}_m = (\bar{v}_{x,m}, \bar{v}_{y,m})$ is the modal acoustic velocity vector, $\mathbf{M}_\infty = \mathbf{V}_\infty / c_0 = (M_\infty, 0)$, and the superscript * indicating the complex conjugate. The x-component of $\mathbf{I}_m$ writes:

$$I_{x,m}(\omega, x, y) = \frac{1}{2}\mathrm{Re}\left\{ \left(\bar{p}_m(\omega, x, y) + M_\infty \bar{v}_{x,m}(\omega, x, y)\rho_0 c_0 \right)^* \left(\bar{v}_{x,m}(\omega, x, y) + M_\infty \frac{\bar{p}_m(\omega, x, y)}{\rho_0 c_0} \right) \right\}, \tag{15}$$

The modal velocity along x, $\bar{v}_{x,m}$, is obtained from the Euler equation of acoustics, projected along x:

$$-\rho_0(\partial_t + U_\infty \partial_x) v_{x,m} = \partial_x p_m. \tag{16}$$

By replacing Eq. (13) in Eq. (16), we obtain:

$$\bar{v}_{x,m}(\omega, x, y) = \frac{A_m}{\rho_0 c_0} \frac{k_{x,m}}{k_0 - M_\infty k_{x,m}} \psi_m(y)\, e^{j\omega t - jk_{x,m}x}. \tag{17}$$

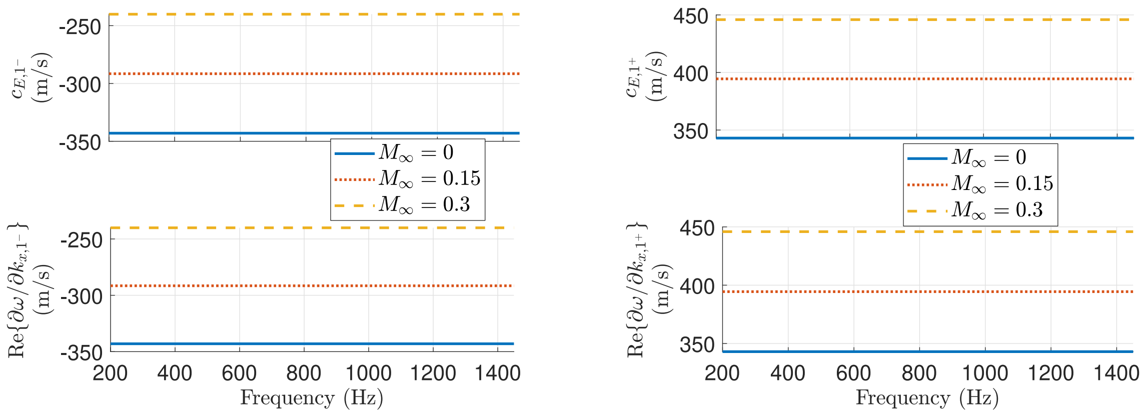

(a) (b)

Fig. 5. Spectra of the modal energy propagation speed $c_{E,m}$ and group velocity in case of hard-walled waveguide, for plane wave 1^- (a) and 1^+ (b), with varying M_∞.

Replacing Eqs. (13) and (17) in Eq. (15), and integrating over the cross-section, we get the average modal acoustic intensity along x:

$$I_{x,m}(x,\omega) = \frac{|A_m|^2}{2h\rho_0 c_0} e^{2\mathrm{Im}\{k_{x,m}\}x} \left[\mathrm{Re}\left\{\frac{k_{x,m}}{k_0 - M_\infty k_{x,m}}\right\}(1 + M_\infty^2) + M_\infty \left|\frac{k_{x,m}}{k_0 - M_\infty k_{x,m}}\right|^2 + M_\infty\right] \int_0^h |\psi_m(y)|^2 \mathrm{d}y. \tag{18}$$

From [5,41], we obtain the average modal kinetic and potential energies, $E_{\mathrm{kin},m}$ and $E_{\mathrm{pot},m}$ respectively, as:

$$\begin{aligned} E_{\mathrm{kin},m}(x,\omega) &= \frac{1}{2h}\int_0^h \mathrm{Re}\left\{\frac{1}{2}\rho_0(\bar{\mathbf{v}}_m^* \cdot \bar{\mathbf{v}}_m) + \bar{p}_m^* M_\infty \frac{\bar{v}_{x,m}}{c_0}\right\}\mathrm{d}y \\ &= \frac{|A_m|^2}{2\rho_0 c_0^2 h} e^{2\mathrm{Im}\{k_{x,m}\}x} \left[\left(\frac{1}{2}\left|\frac{k_{x,m}}{k_0 - M_\infty k_{x,m}}\right|^2 + M_\infty \mathrm{Re}\left\{\frac{k_{x,m}}{k_0 - M_\infty k_{x,m}}\right\}\right)\int_0^h |\psi_m(y)|^2 \mathrm{d}y \right. \\ &\quad \left. + \frac{1}{2|k_0 - M_\infty k_{x,m}|^2}\int_0^h |\partial_y \psi_m(y)|^2 \mathrm{d}y\right] \end{aligned} \tag{19}$$

$$E_{\mathrm{pot},m}(x,\omega) = \frac{1}{4\rho_0 c_0^2 h}\int_0^h \bar{p}_m^* \bar{p}_m \mathrm{d}y = \frac{|A_m|^2}{4\rho_0 c_0^2 h} e^{2\mathrm{Im}\{k_{x,m}\}x} \int_0^h |\psi_m(y)|^2 \mathrm{d}y \tag{20}$$

Assuming isentropic (or adiabatic) flow, then $E_{\mathrm{tot},m} = E_{\mathrm{kin},m} + E_{\mathrm{pot},m}$. Hence, from Eqs. (18), (19) and (20), we can retrieve the modal energy propagation speed along x, defined as:

$$c_{E,m}(\omega) = \frac{I_{x,m}(x,\omega)}{E_{\mathrm{tot},m}(x,\omega)} = \frac{I_{x,m}(x,\omega)}{E_{\mathrm{kin},m}(x,\omega) + E_{\mathrm{pot},m}(x,\omega)}, \tag{21}$$

where the x-dependency disappears in $c_{E,m}$, because numerator and denominator share the same function of x: $e^{2\mathrm{Im}\{k_{x,m}\}x}$. The sign of $c_{E,m}$ will inform us about the direction of propagation of the acoustic mode m (toward $+x$ if positive). The $\mathrm{Im}\{k_{x,m}\}$ instead, gives the attenuation (or amplification) rate of the modal acoustic intensity along the duct mode x-propagation, as it can be seen from Eq. (18). For a lossless waveguide, the modal energy propagation speed $c_{E,m}$ coincides with the group velocity $\mathrm{Re}\{\partial\omega/\partial k_{x,m}\}$ [42].

In Fig. 5, we show the variation of $c_{E,m}$ and $\mathrm{Re}\{\partial\omega/\partial k_{x,m}\}$ with M_∞ for the plane wave modes propagating towards $-x$ (mode 1^-) and $+x$ (mode 1^+), in a hard-wall case. It is easy to verify that $c_{E,m} \equiv \mathrm{Re}\{\partial\omega/\partial k_{x,m}\}$. The spectra are focused in the frequency range [200, 1450] Hz to comply with the limits employed in the experimental testing. Notice that the cut-on frequency of the first duct-mode higher than the plane wave, for a hard-walled waveguide of cross-section height 0.111 m, without mean-flow, is $f_1 = 1545$ Hz. The cut-on frequencies, in case of a hard-walled 2D waveguide with flow, are given by $f_m = m\frac{c_0}{2h}\sqrt{1 - M_\infty}$, with m any positive integer [5].

In the following, we analyse the dispersion solutions in a waveguide lined only on the top by the ABL (as in Fig. 3), in presence of mean-flow, and in the plane wave regime of the corresponding hard-walled waveguide.

The local impedance component ζ_{Loc} of the ABL is a SDOF resonator, which is also the case for most of the actual tunable liners, as the ERs. The mass and stiffness terms of ζ_{Loc} are taken proportional to the acoustic mass and stiffness of the open-circuit ER prototype employed in the experimental test-bench of Section 5, while the resistance term is taken as a fraction of the characteristic air impedance $\rho_0 c_0$. This convention follows the one provided in [12]. Hence:

$$\zeta_{\mathrm{Loc}}(\mathrm{j}\omega) = \frac{1}{\rho_0 c_0}\left(M_d \mathrm{j}\omega + R_d + \frac{K_d}{\mathrm{j}\omega}\right), \tag{22}$$

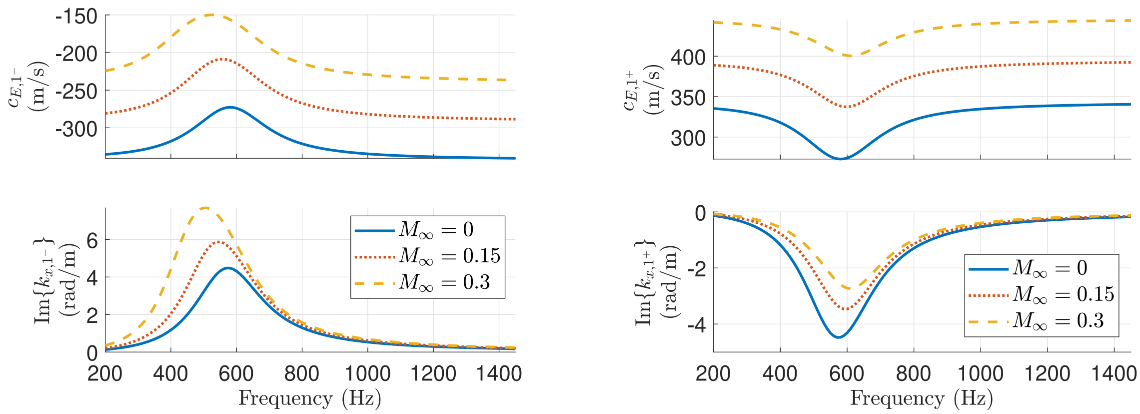

(a) (b)

Fig. 6. Spectra of the modal energy propagation speed $c_{E,m}$ and $\mathrm{Im}\{k_{x,m}\}$ in case of ABL lining the top boundary of the waveguide with $M_b = 0$, $\mu_M = 0.5$, $f_d = 600$ Hz and $r_d = 1$, and varying M_∞ for mode 1^- (a), and for mode 1^+ (b).

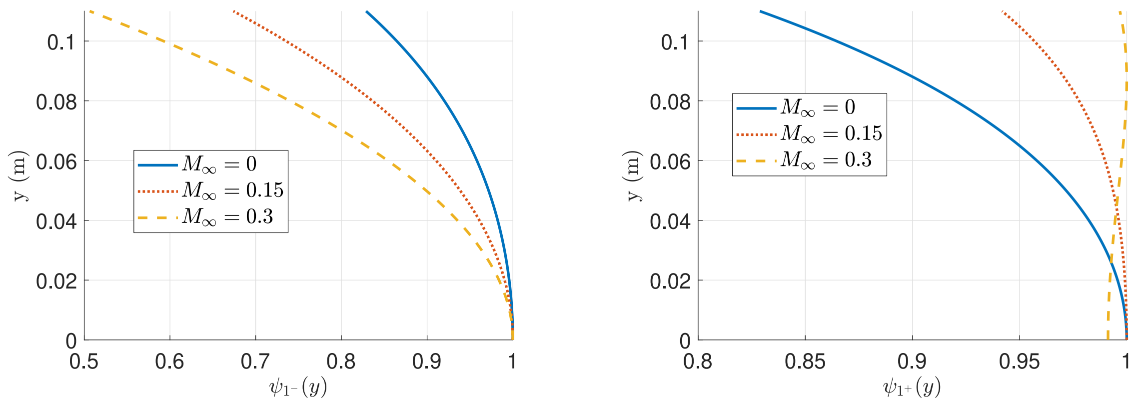

(a) (b)

Fig. 7. Duct-mode shapes in case of ABL lining the top boundary of the waveguide, with $M_b = 0$, $\mu_M = 0.5$ and $r_d = 1$, for mode 1^- (a) and 1^+ (b) at $f_d = 600$ Hz, with varying M_∞.

Table 1
Thiele-Small parameters of the ER.

Model parameters	M_0	R_0	K_0	Bl/S_e
Units	kg/m^2	Pa s/m	Pa/m	Pa A^{-1}
Values	0.401	199.48	6.07×10^6	1.25×10^3

where $R_d = r_d \rho_0 c_0$ is the desired resistance, while the desired reactive components are defined as $M_d = \mu_M M_0$ and $K_d = \mu_K K_0$, with M_0 and K_0 the acoustic mass and stiffness of the open-circuit ER prototype employed in the experimental test-bench of Section 5. Their values are reported in Table 1. The resonance frequency f_d of ζ_{Loc} can be varied by tuning either the stiffness μ_K or the mass μ_M parameters, as $f_d = f_0\sqrt{\mu_K/\mu_M}$, with f_0 being the resonance frequency of the open-circuit ER (619 Hz).

Fig. 6(a) shows the energy propagation speed along x of mode 1^-, along with $\mathrm{Im}\{k_{x,1^-}\}$, in case of $\mu_M = 0.5$, $r_d = 1$, $f_d = 600$ Hz, for three values of M_∞. Notice how, by increasing M_∞, the attenuation rate of the upstream propagating mode 1^- increases. Fig. 6(b) shows the same spectra but for mode 1^+, showing a reduction of the attenuation rate with increasing M_∞. Fig. 7 shows the duct-mode shape evolution of modes 1^- and 1^+ with M_∞, at $f_d = 600$ Hz. Each mode shape m is normalized to its absolute maximum: $\max_y\{|\psi_m(y)|\}$. It is evident how, the upstream propagating mode 1^- gets more and more curved as M_∞ increases, while the opposite happens for mode 1^+. Indeed, the mean-flow tends to reduce the effect of the locally-reacting liner on the downstream propagating mode, which almost approaches a plane wave solution. This non-reciprocal behaviour is naturally induced by the presence of a mean-flow $M_\infty \neq 0$, in a waveguide lined by a locally-reacting liner. In this regard, it is significant to remind that, in [12], it

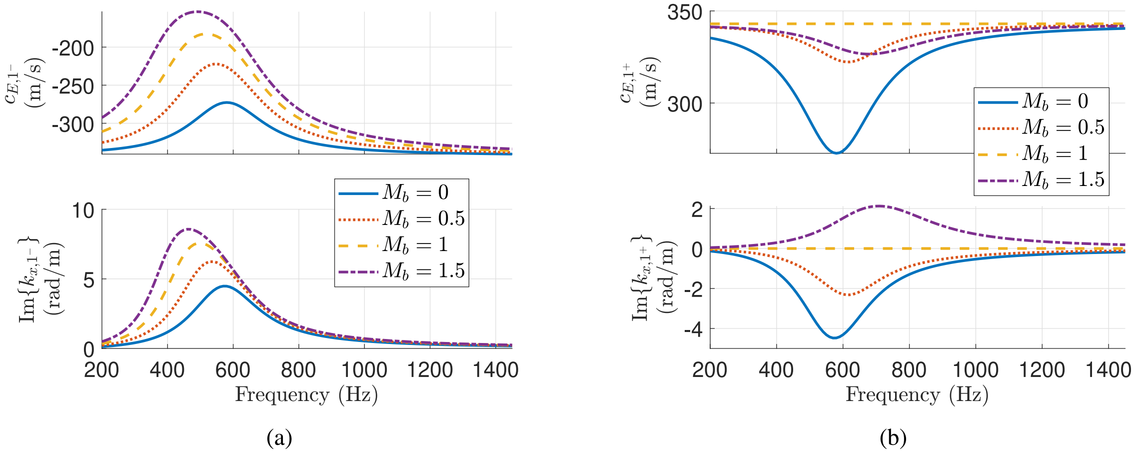

Fig. 8. Spectra of the modal energy propagation speed $c_{E,m}$ and $\mathrm{Im}\{k_{x,m}\}$, in case of $M_\infty = 0$ and ABL lining the top boundary of the waveguide with $\mu_M = 0.5$, $r_d = 1$, and varying M_b, for mode 1^- (a), and mode 1^+ (b).

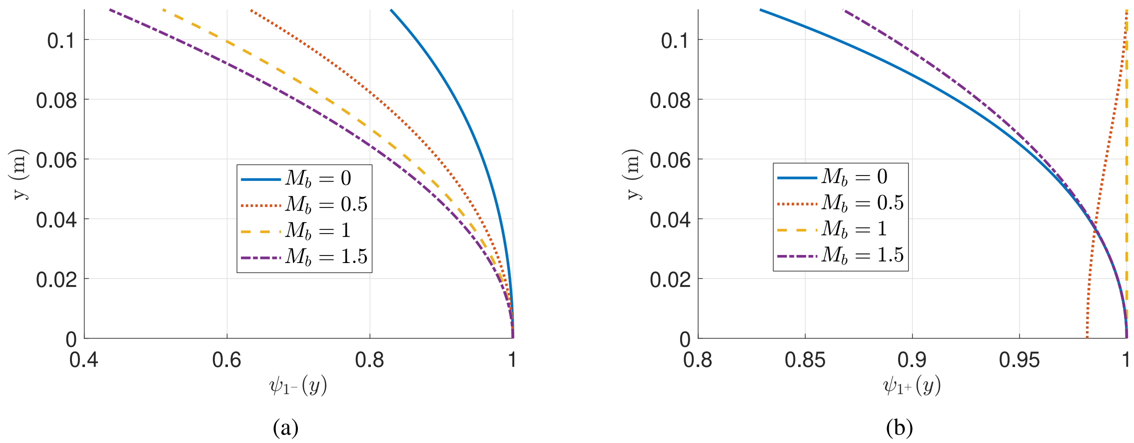

Fig. 9. Duct-mode shapes in case of $M_\infty = 0$ and ABL lining the top boundary of the waveguide with $\mu_M = 0.5$, $r_d = 1$, and varying M_b, for mode 1^- (a), and mode 1^+ (b). at $f_d = 600$ Hz.

was pointed out that, for what concerns duct modes, a boundary advection speed M_b (without airflow) had similar effects as a mean-flow M_∞ in a duct with locally-reacting liners: as M_∞ favours the downstream propagation and mainly opposes the upstream one, analogous results are obtained if the mean-flow M_∞ is replaced by a boundary advection speed M_b on a duct lined by the ABL. This is evident by comparing Figs. 6 and 7, with Figs. 8 and 9. Indeed, Figs. 8 and 9 are the dispersion solutions of modes 1^- and 1^+ in case of $M_\infty = 0$ and varying M_b. From Figs. 8(b) and 9(b), notice the perfect non-reciprocal behaviour achieved for $M_b = -1$, when mode 1^- becomes a perfect plane wave while mode 1^+ is significantly attenuated around f_d. Instead, for $M_b = 1.5$, mode 1^+ becomes unstable ($c_{I,1^+}$ and $\mathrm{Im}\{k_{x,1^+}\}$ have the same sign, check Fig. 4), as known from [12].

So far, the ABL with $M_b \neq 0$, has never been confronted with the presence of a mean-flow $M_\infty \neq 0$. After having analysed the effect of M_∞ in case of a purely locally-reactive liner ($M_b = 0$), and the effect of M_b in absence of mean flow ($M_\infty = 0$), we can now study the effect of the combination of $M_\infty \neq 0$ and $M_b \neq 0$ upon the least attenuated duct modes.

Fig. 10 shows the enhancement of attenuation of modes 1^+ and 1^- around $f_d = 600$ Hz, when an M_b with opposite sign of $c_{E,m}$ is applied. This enhancement increases as higher is $|M_b|$, and enlarges the bandwidth towards lower frequencies, though f_d is unchanged. Notice the highly non-reciprocal behaviour around f_d, when M_b approaches $1+M_\infty$ or $-1+M_\infty$. However, contrary to the case without mean-flow reported in [12], perfect non-reciprocity is never achievable, because $k_{x,1\pm} = \pm k_0/(1 \pm M_\infty)$ and $\psi_{1\pm}(y) = 1$, are never solutions of the eigenvalue problem of Eq. (A.3). Fig. 10 also shows that, for certain values of M_b, the $\mathrm{Im}\{k_{x,1\pm}\}$ changes its sign, leading to unstable duct-mode propagation. Fig. 11 shows the spectra of $c_{E,m}$ and $\mathrm{Im}\{k_{x,m}\}$ in case of ABL lining the top boundary of the waveguide, in case of $M_\infty = 0.15$, with $\mu_M = 0.5$, $f_d = 600$ Hz and $r_d = 1$, and varying M_b around the limit of stable propagation of mode 1^- **(a, b)**, and 1^+ **(c)**. Notice that the range of M_b for acoustical passivity in open field $[-1 + M_\infty, 1 + M_\infty]$, found in Section 2, gives a good estimation of the stability range of modes 1^+ and 1^-.

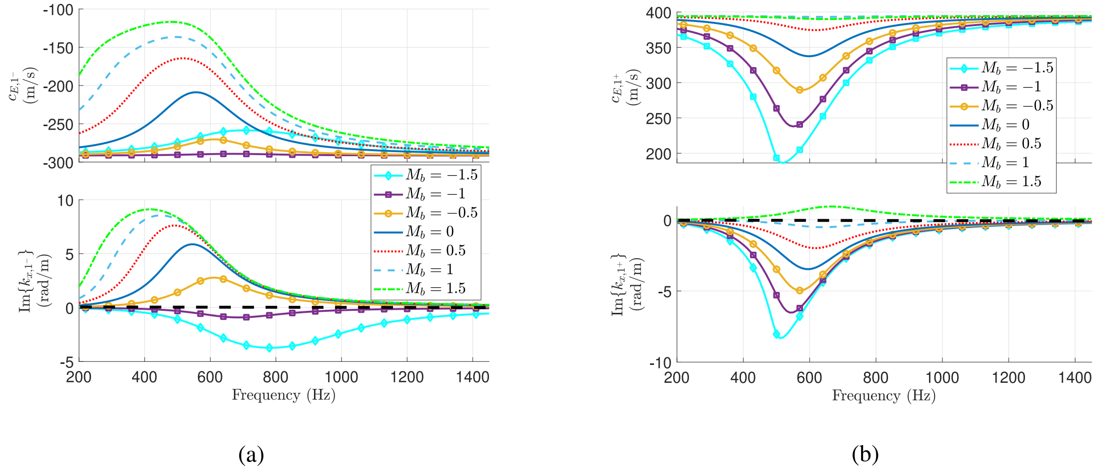

Fig. 10. Spectra of the modal energy propagation speed $c_{E,m}$ and $\mathrm{Im}\{k_{x,m}\}$ in case of ABL lining the top boundary of the waveguide, in case of $M_\infty = 0.15$, with $\mu_M = 0.5$, $f_d = 600$ Hz and $r_d = 1$, and varying M_b, for mode 1^- (a), and for mode 1^+ (b). In dashed black the axis $\mathrm{Im}\{k_{x,m}\} = 0$.

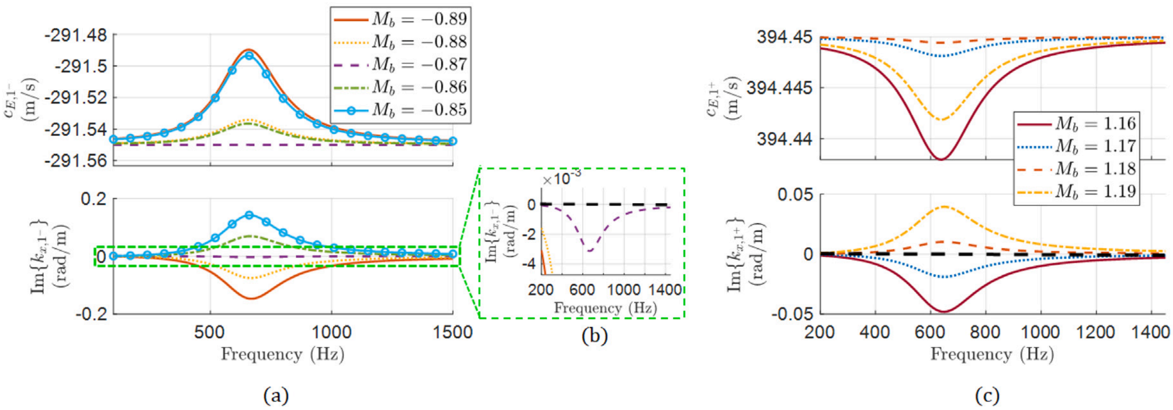

Fig. 11. Spectra of $c_{E,m}$ and $\mathrm{Im}\{k_{x,m}\}$ in case of ABL lining the top boundary of the waveguide, in case of $M_\infty = 0.15$, with $\mu_M = 0.5$, $f_d = 600$ Hz and $r_d = 1$, and varying M_b around the limit of stable propagation of mode 1^- (a), and 1^+ (c). In (b), a zoom around the zero level of $\mathrm{Im}\{k_{x,1^-}\}$. In dashed black the axis $\mathrm{Im}\{k_{x,m}\} = 0$.

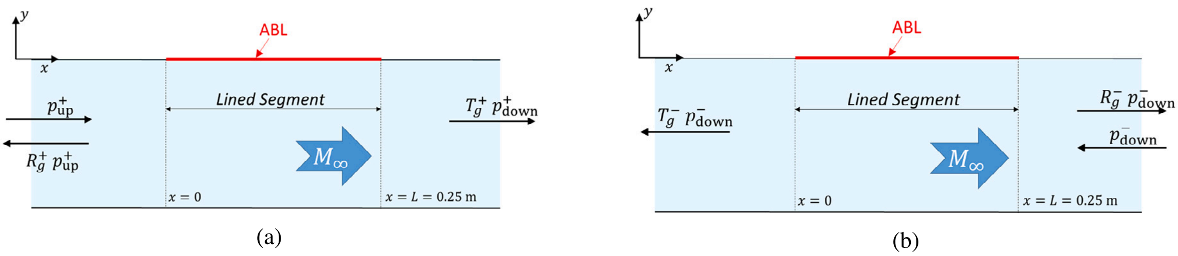

Fig. 12. Lining segment and scattering coefficients definition in a 2D waveguide lined on the upper side by the ABL.

4. Scattering simulations in 2D waveguide

In this section the ABL is analysed in terms of scattering performances in the plane wave regime of a 2D hard-walled waveguide of section $h = 0.111$ m, lined on the upper boundary for a length of 0.25 m. The waveguide domain is modelled by a convected wave

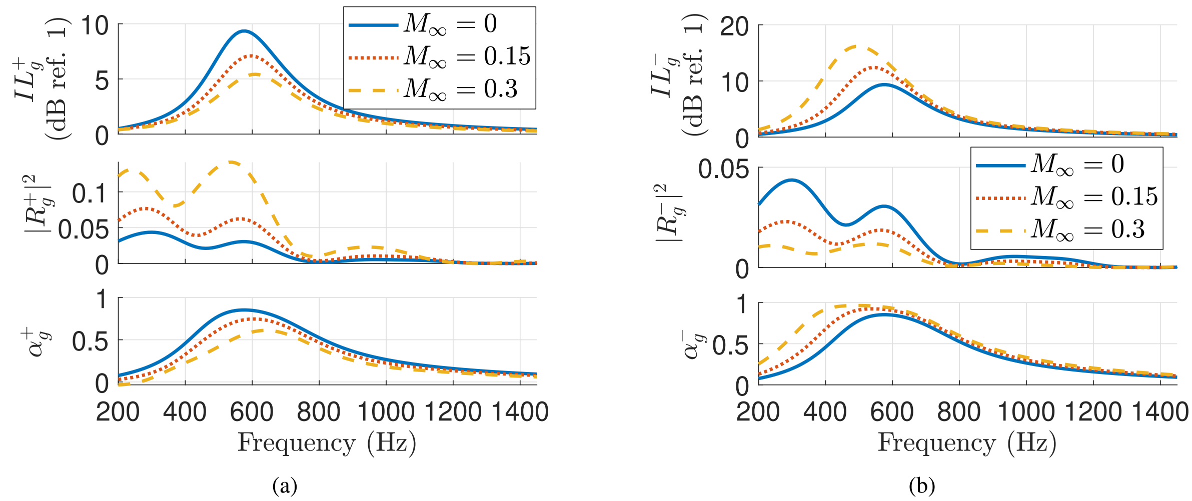

Fig. 13. Scattering coefficients in a 2D waveguide of cross section width $h = 0.111$ m with lined segment of length $L = 0.25$ m, lined on top by the ABL with $r_d = 1$, $\mu_M = 0.5$, $f_d = 600$ Hz, $M_b = 0$, and varying M_∞.

equation, with an inviscid and irrotational background mean-flow of $M_\infty < 1$ as in Section 3. The scattering problem is illustrated in Fig. 12, where the reflection R_g and transmission T_g coefficients are defined for incident field directed toward either $+x$ or $-x$. The subscript g is employed to differentiate the present *grazing* incidence from the oblique incidence scattering of Section 2. The ABL is applied continuously on the boundary of the waveguide in the lined segment. The scattering matrix is defined in Eq. (23) for the plane wave regime of a hard-walled duct.

$$\begin{bmatrix} p^+_{\mathrm{down}} \\ p^-_{\mathrm{up}} \end{bmatrix} = \begin{bmatrix} T^+_g & R^-_g \\ R^+_g & T^-_g \end{bmatrix} \begin{bmatrix} p^+_{\mathrm{up}} \\ p^-_{\mathrm{down}} \end{bmatrix}. \tag{23}$$

The superscript signs + or − in Eq. (23), indicate the direction of propagation of the incident plane wave (toward either $+x$ or $-x$). The results in terms of scattering matrix coefficients, have been obtained by FE simulations in COMSOL Multiphysics. As in the duct mode analysis, the FE mesh has been built sufficiently fine to fully resolve both longitudinal and transversal pressure fields up to $f_{max} = 1.45$ kHz. The scattering coefficients $T_g^\pm$ and $R_g^\pm$ are computed, by exciting first the left and then the right termination. The scattering performances are presented in terms of power scattering coefficients for both positive and negative propagation. The power scattering coefficients are defined from the power balance [43] which, in case of plane waves, reduces to:

$$1 = \alpha_g^\pm + |T_g^\pm|^2 + |R_g^\pm|^2, \tag{24}$$

where α_g is the absorption coefficient in grazing incidence. From $|T_g^\pm|^2$, it is possible to compute the Transmission Loss $(TL_g^\pm)_{Liner} = 10\log_{10}(1/|T_g^\pm|^2)$, and the Insertion Loss $IL_g^\pm = (TL_g^\pm)_{Liner} - (TL_g^\pm)_{Rigid}$. As $(TL_g^\pm)_{Rigid} = 0$ in simulations, $IL_g^\pm = (TL_g^\pm)_{Liner}$.

Fig. 13 shows the power scattering coefficients in case of $r_d = 1$, $\mu_M = 0.5$, $M_b = 0$, in case of three different M_∞. Notice how the $IL_g^\pm$ follows the same trends as the $\mathrm{Im}\{k_{x,1\pm}\}$ of Fig. 6. The tight correlation between $IL_g^\pm$ and $\mathrm{Im}\{k_{x,1\pm}\}$ is evident also in Fig. 14 (to be compared with Fig. 8), where $M_\infty = 0$ and M_b is varied. Hence, by looking at Figs. 13 and 14, the analogous effect of varying M_∞ and M_b upon the isolation performances is confirmed also in terms of scattering coefficients.

From Fig. 14(b), we remark that, the presence of a synthetic advection speed $M_b > 0$, leads to higher IL_g^- compared to the classical local impedance ($M_b = 0$), both in peak and bandwidth of efficient noise isolation. The optimization of the ABL is out of the scope of the present paper. Nevertheless, Appendix B presents a brief comparison of the isolation performances obtained by the ABL and the classical benchmark of the Cremer impedance, demonstrating, once again, the potentiality of the ABL to go beyond the state-of-art.

The effect of varying M_b in presence of a $M_\infty \neq 0$ is showed in Fig. 15. First of all, we notice the fear agreement between the $\mathrm{Im}\{k_{x,1-}\}$ ($\mathrm{Im}\{k_{x,1+}\}$) of Fig. 10(a) (Fig. 10(b)), and the IL_g^- (IL_g^+) of Fig. 15(b) (Fig. 15(a)), confirming the tight correlation of isolation, non-reciprocity and passivity in the plane wave regime, with the dispersion solutions of the least attenuated duct modes, even in presence of a mean-flow $M_\infty \neq 0$. As far as isolation performances are concerned, increasing $|M_b|$ in opposite sign with respect to the direction of propagation meant to be attenuated, improves isolation. About non-reciprocity, it is evident how for $M_b = 1$ ($M_b = -1$), which is close to $1+M_\infty$ ($1-M_\infty$), we obtain very good transmission towards $+x$ ($-x$) while high isolation towards $-x$ ($+x$). Concerning acoustical passivity, we can still detect that IL_g^+ and α_g^+ (IL_g^- and α_g^-) are negative for $M_b = 1.5$ ($M_b = -1$ and $M_b = -1.5$), in full coherence with the duct-mode simulations of Fig. 10. Nevertheless, we also notice some behaviours which are not predicted by the least-attenuated duct-mode simulations, therefore probably relating to the participation of higher-order duct-modes at the left and right interfaces of the lined segment with the rigid portions of the duct. For example, $|R_g^+|$ is higher than 1 in the frequency range between 910 and 1075 Hz, for $M_b = -1.5$, hence leading to an $\alpha_g^- < 0$ in the same frequency band. A full

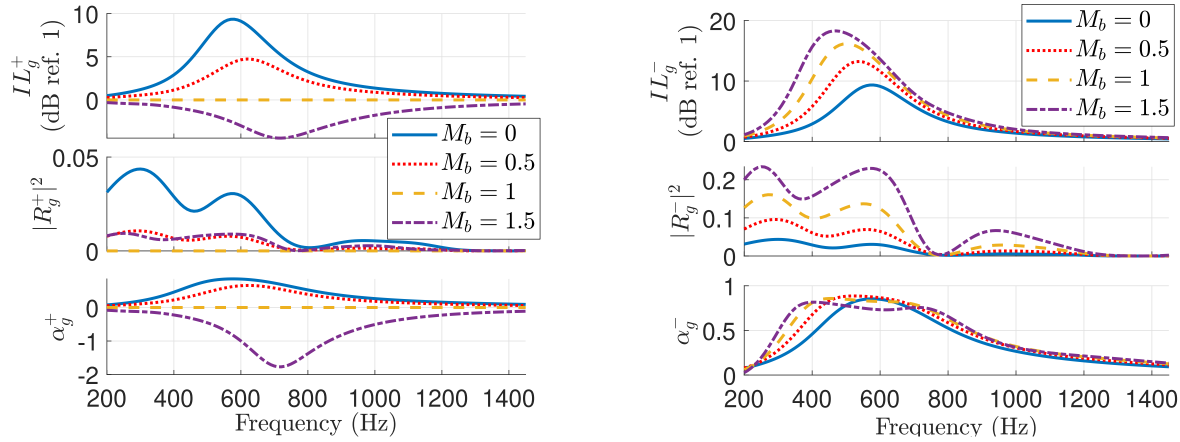

(a) (b)

Fig. 14. Scattering coefficients in case of $M_\infty = 0$, with ABL parameters $r_d = 1$, $\mu_M = 0.5$, $f_d = 600$ Hz, and varying M_b.

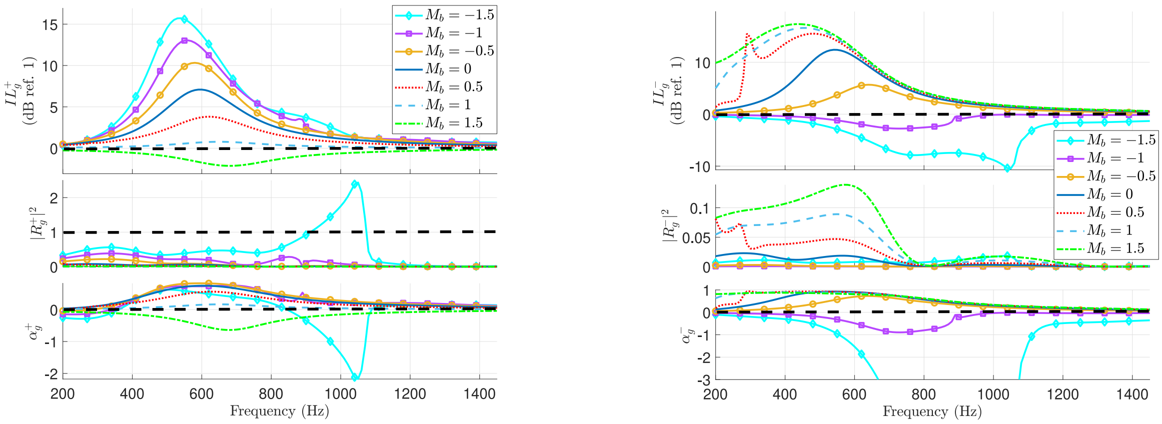

(a) (b)

Fig. 15. Scattering coefficients in case of $M_\infty = 0.15$, with ABL parameters $r_d = 1$, $\mu_M = 0.5$, $f_d = 600$ Hz, and varying M_b.

understanding of such occurrence would require a detailed mode-matching analysis for the scattering evaluation, which is beyond the scope of the present paper. Nevertheless, we can speculate that $M_b = -1.5$ is much beyond the stability limit of mode 1^- (which is between $M_b = -0.86$ and $M_b = -0.87$ as showed in Fig. 11), therefore entailing a significant $\mathrm{Im}\{k_{x,1^-}\} < 0$, as showed in Fig. 10(a). This means that even a small participation of mode 1^- in the backward reflection at the left interface between the rigid and lined segments, can induce a high reflection coefficient. Another unexpected result is α_g^+ becoming slightly negative for frequencies lower than 360 Hz, in case of $M_b = -1$ and -1.5. This time, the negative α_g^+ is not accompanied by either $IL_g^+ < 0$ or $|R_g^+| > 1$, but is the combination of reflected and transmitted energy which overcomes the incident one, therefore leading to an $\alpha_g^+ < 0$, according to Eq. (24). Notice that these specific passivity issues were not encountered in [12], where no mean-flow was considered. Moreover, these unexpected behaviours at some frequencies, only happen when M_∞ and M_b have opposite signs, which might also suggest the impact of introducing a negative boundary convection upon a positively convected air-domain, which might introduce surface waves. A full analysis of these special behaviours is not required at this stage. In fact, the contact between the boundary convection introduced by the ABL, and the convected air-domain, is not featured in the actual experimental setup presented in Section 5, where a wiremesh, supported by a perforated plate, separate the convected air-domain from the EL interface.

The 2D simulations reported in the present section and in Section 3, highlight the potentialities of the ABL in terms of noise isolation and non-reciprocal propagation also in presence of airflow. These results give us sufficient confidence to experimentally implement the ABL in an actual convected waveguide, as done in the following section.

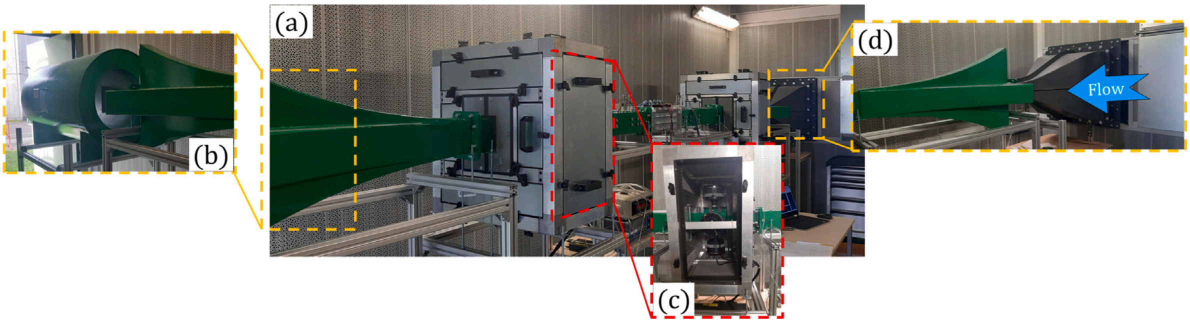

Fig. 16. CAIMAN wind tunnel available at the LMFA of ECL: Entire view (a), with downstream anechoic termination and silencer (b), internal view of the pneumatic sources (c) applied both upstream and downstream the lined segment, convergent flow-inlet and the attached upstream anechoic termination (d).

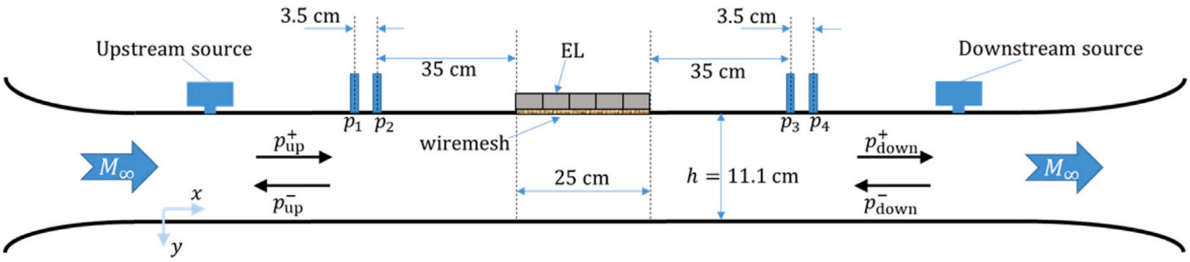

Fig. 17. Schematics of the CAIMAN test-rig.

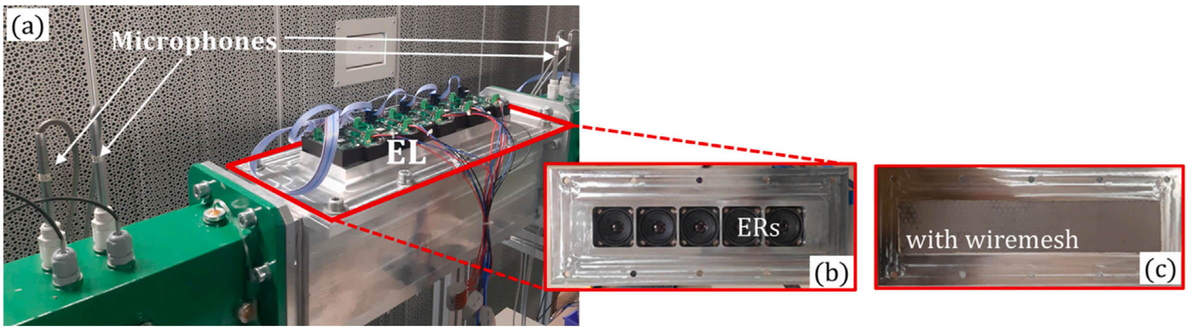

Fig. 18. Lined segment of the waveguide (a), with the EL applied on top, upstream and downstream microphones for the scattering evaluation; in (b) a photo of the EL and in (c) the EL covered by wiremesh.

5. Experimental results

In this section, the ABL is experimentally tested on an array of 5 ER prototypes lining the central segment of a waveguide with rectangular cross-section of size 0.111×0.07 m. The waveguide is the CAIMAN wind-tunnel [44] of the LMFA in the ECL, illustrated in Fig. 16a. In Fig. 16b and c, the downstream and upstream terminations are focused, with their exponential shape to minimize reflections. The upstream termination is preceded by the convergent flow-inlet, while the downstream termination is followed by a silencer to minimize the noise radiated outside. The pneumatic sources are placed into two boxes, as showed in Fig. 16c, both upstream and downstream the lined segment and sufficiently far from the microphones for neglecting evanescent waves (according to [45]). The overall geometry of the test-bench is resumed in the schematics of Fig. 17. The lined segment is focused in Fig. 18a. The EL composed of 5 ERs is showed in Fig. 18b without the covering wiremesh, and in Fig. 18c with the frontal wiremesh (supported by a perforated plate) needed in order to protect the ERs from the flow. The acoustic properties describing the wiremesh as a porous medium [46] are detailed in Table 2 as reported in [7], referring to the wiremesh I130, and its thickness is 0.151 mm.

The photo in Fig. 19a shows the front side of the ER, equipped by a loudspeaker and 4 surrounding microphones (A, B, C and D), to retrieve an estimation of the pressure $\hat{p}$ and its x-derivative $\hat{\partial}_x p$ on the speaker diaphragm. The control strategy is unchanged with respect to [12], but is resumed here for sake of clarity. It is based on model-inversion [16,36] and employs the loudspeaker

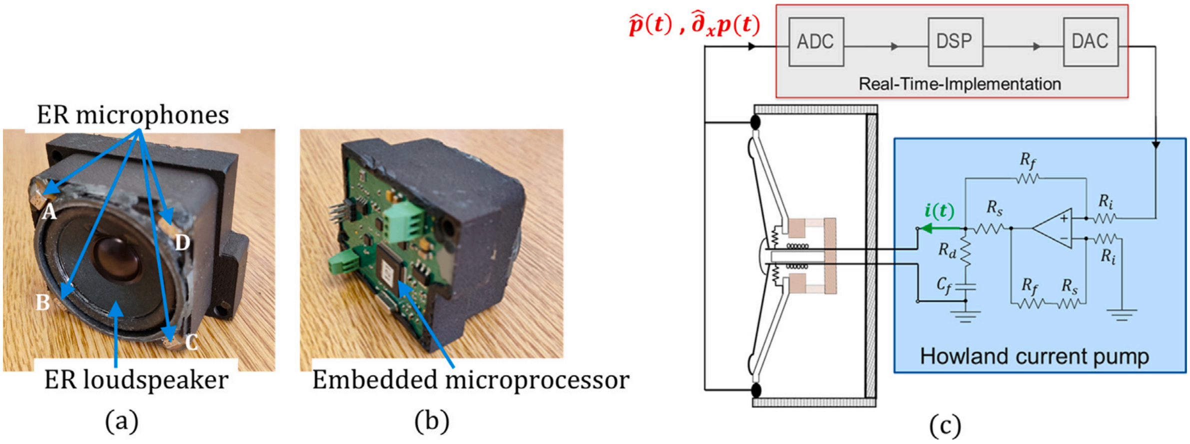

Fig. 19. ER prototype frontal (a) and rear (b) views, and schematics of the control architecture (c).

Table 2
Model parameters of the ER.

Wiremesh parameters	Flow resistivity	Porosity	Tortuosity	Viscous length	Thermal length
Units	rayls/m = Pa s/m^2	–	–	–	–
Values	2.7×10^6	0.4	1.3	0.2	1

Thiele-Small SDOF model [47] reported in Eq. (25), in terms of the Laplace variable s:

$$Z_0(s)\bar{v}(s) = \bar{p}(s) - \frac{Bl}{S_e}\bar{i}(s). \tag{25}$$

In Eq. (25), $\bar{p}(s)$ and $\bar{v}(s)$ are the acoustic pressure and velocity, respectively, on the speaker diaphragm, $\bar{i}(s)$ is the electrical current in the speaker coil, $Z_0(s) = M_0 s + R_0 + K_0/s$ is the acoustical impedance of the loudspeaker in open circuit, with M_0, R_0 and K_0 the corresponding acoustical mass, resistance and stiffness. The electrical current $\bar{i}(s)$ is multiplied by the force factor Bl to get the electromagnetic force, and divided by the effective area S_e to retrieve an equivalent pressure. Observe that the impedance description of Eq. (25) is a lumped-element model, which is reliable as long as the wavelength of the acoustic field is sufficiently larger than the size of the speaker diaphragm. This is true for any local impedance modelling. The upper frequency of validity of the lumped-element assumption is much beyond the frequency range of validity of the SDOF loudspeaker-model, which lies around the first speaker mode (around 600 Hz). Therefore, both the lumped-element assumption and the SDOF model are valid around the principal resonance of the ERs.

The ABL is implemented by defining the electrical current $i(s)$ as in Eq. (26):

$$i(s) = H_{\mathrm{Loc}}(s)\hat{\bar{p}}(s) + H_{\mathrm{grad}}(s)\hat{\partial}_x\bar{p}(s), \tag{26}$$

where $\hat{\bar{p}}(s)$ and $\hat{\partial}_x\bar{p}(s)$ are the estimated local pressure and its x-derivative on each speaker diaphragm, in the Laplace domain. The local sound pressure is estimated by averaging the four microphones' signals $\hat{p} = (p_A + p_B + p_C + p_D)/4$, while the x-derivative is estimated by a first-order finite difference $\hat{\partial}_x p = \Big((p_C + p_D) - (p_A + p_B)\Big)/\Delta x$, with Δx the distance between the microphones before (A, B) and after (C, D) each ER speaker, along the x-direction.

The transfer functions $H_{\mathrm{Loc}}(s)$ and $H_{\mathrm{grad}}(s)$ are obtained by equating the velocity of the speaker diaphragm $\bar{v}$ to $s\bar{u}_y$, where $\bar{u}_y$ the normal displacement given by Eq. (7) with $s = \mathrm{j}\omega$. Hence, we get the expressions in the Laplace space of H_{Loc} and H_{grad}, in Eqs. (27) and (28), respectively.

$$H_{\mathrm{Loc}}(s) = \frac{S_e}{Bl}\left(1 - \frac{Z_0(s)}{Z_{\mathrm{Loc}}(s)}\right), \tag{27}$$

$$H_{\mathrm{grad}}(s) = -\frac{S_e}{Bl}\frac{Z_0(s)}{Z_{\mathrm{Loc}}(s)}\frac{U_b}{s}F_{hp}(s), \tag{28}$$

where $F_{hp}(s)$ in $H_{\mathrm{grad}}(s)$ is a high-pass filter necessary in order for $H_{\mathrm{grad}}(\mathrm{j}\omega)$ not to become infinite for $\omega \to 0$. The Thiele-Small parameters appearing in Eq. (25), and listed in Table 1, are identified by acoustic measurements, as described in [48]. Further details upon such control strategy can be found in [17,36].

Each ER is controlled autonomously, and the control architecture is illustrated in Fig. 19c: the signals $\hat{p}$ and $\hat{\partial}_x p$ on the speaker diaphragm, after being digitally converted by the Analogue-Digital-Converter (ADC), are fed into a *programmable* digital signal processor (DSP) where the output of the control is computed at each time step. The Howland current pump [49] allows to enforce the electrical current i in the speaker coil independently of the voltage at the loudspeaker terminals. It consists of an operational

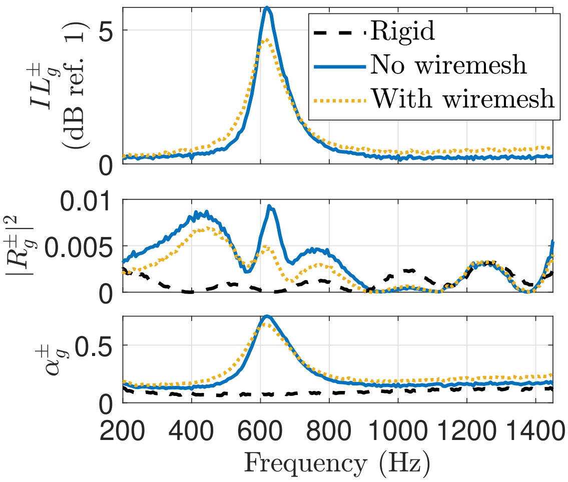

Fig. 20. Effect of wiremesh on the scattering coefficient, in case of $M_\infty = 0$, and ABL with $M_b = 0$, $r_d = 1$, $\mu_M = 0.5$, and $f_d = f_0$.

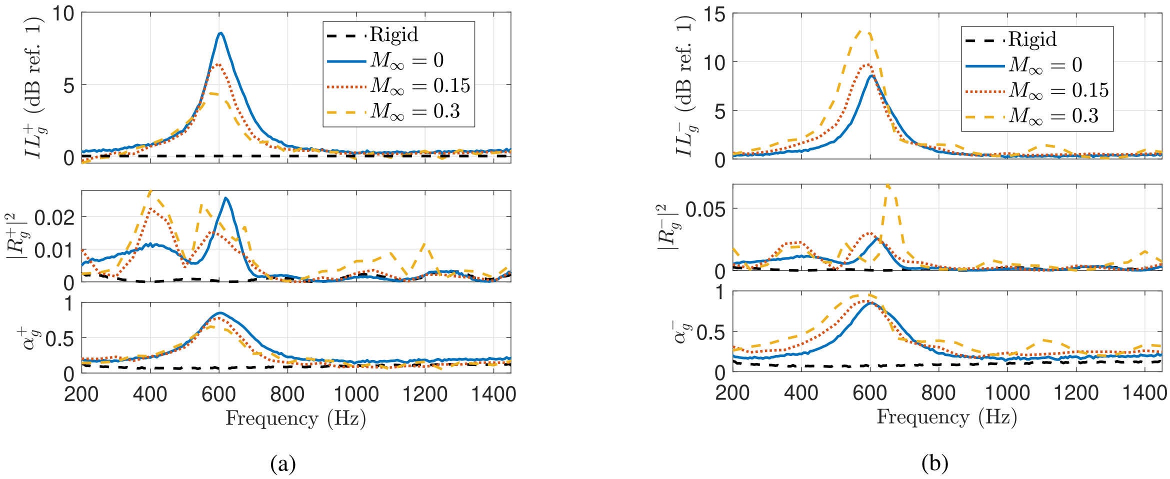

Fig. 21. Experimental scattering coefficients, in case of ABL parameters $r_d = 0.25$, $\mu_M = 0.5$, $f_d = f_0$ Hz, and $M_b = 0$, and with varying M_∞.

amplifier, two input resistors R_i, two feedback resistors R_f, and a current sense resistor R_s. The resistance R_d and capacitance C_f constitutes the compensation circuit to ensure stability with the grounded load [50]. The digital processing instructions are downloaded on the embedded microprocessor (shown in Fig. 19b) from an external interface communicating directly with the user laptop, where the desired control law is defined.

The four scattering coefficients have been estimated according to the two-source method [51]. The excitation signal for the acoustic sources is a band-limited white-noise in case of $M_\infty = 0$, or pure tones (by frequency steps of 25 Hz) in case of $M_\infty \neq 0$ (in order to maximize the signal-to-noise ratio). In both cases, the frequency spectrum covered by the excitation signals is between 200 to 1450 Hz. The high frequency limit assures to be sufficiently below the cut-on frequency of the first higher duct-mode (1545 Hz), while the low frequency limit is to avoid the impact of structural vibrations in the acoustic pressure measurements. The scattering coefficients are plotted along with the ones measured in the benchmark configuration, where the liner is replaced by a rigid wall. The inevitable dissipation of the rigid benchmark appears as very low values of reflection and absorption coefficients. The Insertion Loss is obtained by subtracting the Transmission Loss of the lined configuration from the one measured in the rigid reference, therefore the Insertion Loss of the rigid benchmark is identically equal to zero.

Fig. 20 shows the effect of the wiremesh on the scattering coefficients, in case of $M_\infty = 0$ and ABL with $r_d = 1$, $\mu_M = 0.5$, $f_d = f_0$ and $M_b = 0$. The effect of the wiremesh is to slightly decrease the Insertion Loss peak (of about 1 dB), to mildly shift its frequency towards lower values, and slightly enlarge the corresponding bandwidth. These effects can be modelled, in a first order approximation, by a small increase of the resistance of an equivalent liner comprising both EL and wiremesh. Indeed, an increase of resistance in the ABL leads to a reduction of the peak and a slight increase of the efficient IL_g bandwidth, as showed both

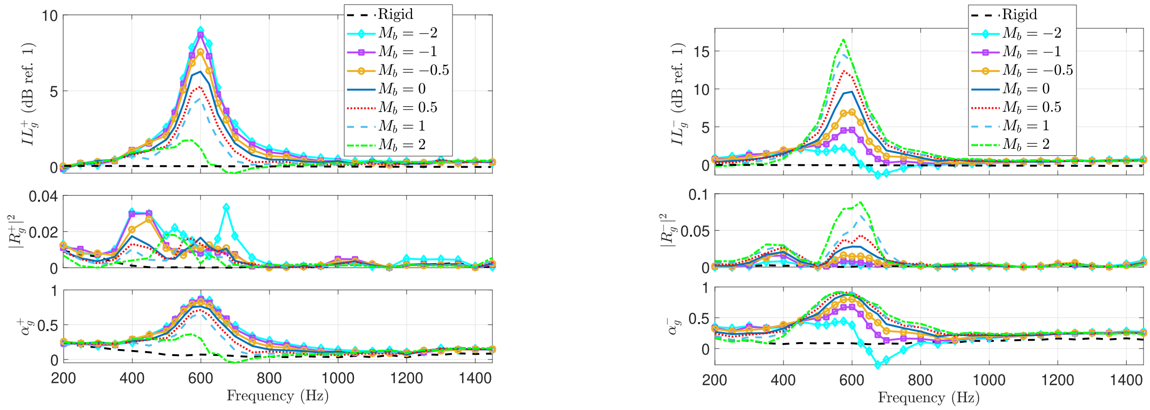

(a) (b)

Fig. 22. Experimental scattering coefficients, in case of $M_\infty = 0.15$, and with ABL parameters $r_d = 0.25$, $\mu_M = 0.5$, $f_d = f_0$, and varying M_b.

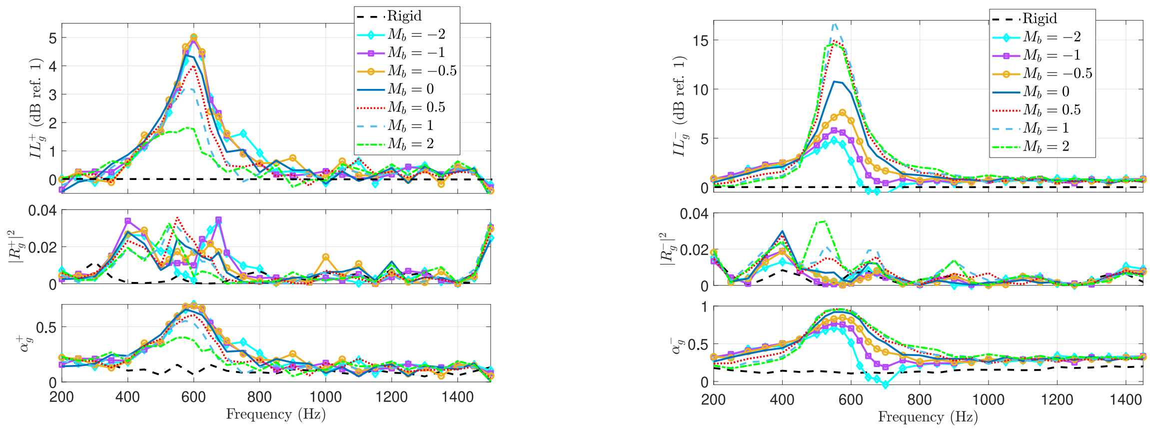

(a) (b)

Fig. 23. Experimental scattering coefficients, in case of $M_\infty = 0.3$, and with ABL parameters $r_d = 0.25$, $\mu_M = 0.5$, $f_d = f_0$, and varying M_b.

numerically and experimentally in [12]. Nevertheless, a full numerical modelling of the experimental setup, comprising EL and wiremesh, is provided and validated in Appendix C.

Fig. 21 shows the scattering coefficients measured with ABL synthesized on the EL, with $M_b = 0$, $r_d = 0.25$ and $\mu_M = 0.5$, in case of varying M_∞. The three different flow Mach numbers are reached by properly setting the rotational speed of the CAIMAN flow-generating fan [44], and measured by hot-wire anemometer. The trends featured by the Insertion Losses follow coherently the ones expected by both 2D scattering simulations (check Fig. 13) and 2D duct-mode analyses (check the $\mathrm{Im}\{k_{x,1\pm}\}$ of Fig. 6). It is evident the natural non-reciprocal behaviour induced by the mean-flow: higher M_∞ enhances noise isolation of the locally-reacting EL for upstream propagation (the IL_g^- peak increases from 8.5 dB at $M_\infty = 0$, to 13.4 dB at $M_\infty = 0.3$), while favouring downstream transmission (IL_g^+ peak decreases from 8.5 dB at $M_\infty = 0$, to 4.3 dB at $M_\infty = 0.3$). Fig. 22 shows the effect of varying M_b when $M_\infty = 0.15$, with $r_d = 0.25$, $\mu_M = 0.5$ and $f_d = f_0$. As expected by 2D duct-mode dispersion solutions (Fig. 10) and 2D scattering simulations (Fig. 15), increasing $|M_b|$ with opposite sign with respect to the direction to isolate, augments the corresponding Insertion Loss, despite the mean-flow. In particular, the IL_g^+ peak can be increased from 6.3 dB for $M_b = 0$ to 9 dB for $M_b = -2$, while the IL_g^- peak can be increased from 9.4 dB for $M_b = 0$ to 16.6 dB for $M_b = 2$.

Notice that, for $M_b = -1$ the simulations predicted a non-passive behaviour of the ABL ($\mathrm{Im}\{k_{x,1^-}\}$ changing sign in Fig. 10(a), while IL_g^- and α_g^- becoming negative in Fig. 15(b)). This is not detected by the experimental scattering curves and is mainly due to the presence of the wiremesh which adds dissipation in the system, therefore increasing the passivity margins of the ABL. However, for $M_b = \pm 2$, the non-passivity of the ABL is still manifested slightly above f_d. Observe that the physiological uncertainties in the loudspeaker model and the time delay of the digital control, prevents the speaker own dynamics to be fully cancelled out by the model-inversion controller. This is responsible of the slight oscillation in frequency of IL_g^+ (IL_g^-) and α_g^+ (α_g^-) for $M_b = -2$ ($M_b = 2$) around resonance (see [12,36]). Fig. 23 shows the same scattering coefficients obtained in case of $M_\infty = 0.3$ with varying M_b. First

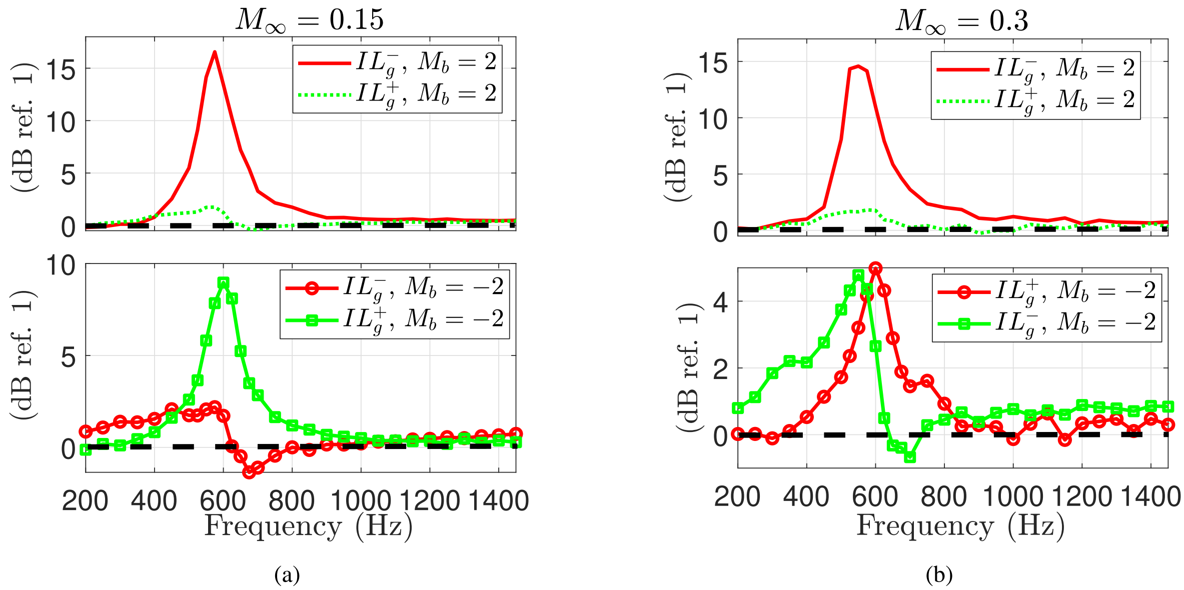

Fig. 24. Experimental Insertion Losses, in case of $M_\infty = 0.15$ (a) and $M_\infty = 0.3$ (b), with ABL parameters $r_d = 0.25$, $\mu_M = 0.5$, $f_d = f_0$, and $M_b = \pm 2$.

of all, notice that, contrary to the case of $M_\infty = 0.15$, reducing M_b below -0.5 does not lead to any significant increase in IL_g^+, whose peak does not overcome 5 dB, compared to the 4.3 dB reached in case of $M_b = 0$. Indeed, as M_∞ augments, it is increasingly harder to oppose the natural reduction of the downstream isolation capability of the liner induced by airflow.

On the other hand, looking at IL_g^-, the ABL isolation is helped by higher M_∞. Indeed, introducing an $M_b > 0$ allows to increase the IL_g^- peak from 10.8 dB for $M_b = 0$, to more than 16 dB for $M_b = 1$. Observe that, increasing M_b from 1 to 2, leads to a reduction of the IL_g^- peak, suggesting the presence of an optimal value of M_b, which should take into account both the EL and the specific wiremesh. A detailed 3D model is provided and validated in Appendix C, for future optimization purposes. As far as passivity is concerned, notice that in case of $M_\infty = 0.3$, an $M_b = 2$ no longer entails a negative IL_g^+ and α_g^+. Indeed, coherently with the discussion in the previous sections, the upper limit on M_b for the ABL acoustical passivity, should increase with M_∞.

Finally, Fig. 24 highlights the non-reciprocal behaviour experimentally accomplished by the ABL. The Insertion Loss corresponding to the two directions of noise transmission are compared for a fixed M_b. If upstream transmission must be avoided, M_b is chosen equal to 2, while an $M_b = -2$ is selected to oppose downstream transmission. The reason why we have chosen such M_b values is that they allowed to achieve highest non-reciprocal propagation while retaining sufficient acoustical passivity. Because of the natural non-reciprocity induced by the mean-flow, it is clear that higher non-reciprocal propagation is obtained when upstream transmission must be opposed, with $(IL_g^- - IL_g^+)$ reaching a peak of 15 dB around f_0 and staying above 5 dB between 500 and 675 Hz. Nevertheless, if the downstream transmission is meant to be contrasted, the ABL is still capable to reverse the natural non-reciprocity induced by the mean-flow for $M_\infty = 0.15$, with $(IL_g^+ - IL_g^-)$ reaching a peak of 7.5 dB and staying above 4 dB between 550 Hz and 650 Hz. A non-reciprocal device which does not exploit the mean-flow (as instead done in [37,38]), but, on the contrary, is capable to induce a non-reciprocal propagation in the opposite sense with respect to the one naturally induced by airflow, is unprecedented to the best of authors' knowledge. However, as already remarked in Fig. 23(a), the efficiency of the liner, and hence of the ABL, is very much weakened at $M_\infty = 0.3$, for which the targeted non-reciprocal propagation when $M_b = -2$ is only mildly achieved in a narrow bandwidth above f_d (see Fig. 24(b)), and reversed for frequencies below f_d. On the other hand, if upstream isolation is targeted with $M_b = 2$, $(IL_g^- - IL_g^+)$ features a peak of about 13 dB and stays above 6 dB from 475 Hz to 675 Hz. The reduction of non-reciprocal performances with M_∞, when $\mathrm{sign}(M_b) = -\mathrm{sign}(M_\infty)$, is physically understandable, as the synthetic advection works only on the boundary, while the mean-flow impact the entire waveguide cross-section. In order to counteract the flow effect, higher synthetic advection speeds should be implemented. Nevertheless, the presence of the wiremesh also limits the potentials of the ABL, which cannot overcome the highest isolation achieved for an optimal M_b.

In this section, the ABL potentials have been experimentally validated against airflows of Mach 0.15 and 0.3. We demonstrated that also in presence of flow, the ABL is still capable of enhancing the isolation of locally-reacting operators. No significant passivity issues have been observed, also thanks to the frontal wiremesh which enlarges the acoustical passivity margins (similarly to the porous layer applied in [36]). On the other hand, the presence of the wiremesh limits the potentials of the synthetic boundary advection. Hence, for optimizing the liner performances, the presence of the wiremesh should be taken into account. This is out of the scope of the present paper, which aims at demonstrating the ABL potentialities in presence of flow, reserving the optimization stage for specific purposes to a dedicated future work. In Appendix C though, a 3D model including the wiremesh, is validated against the measured scattering coefficients and provides an useful tool for future optimizations. Finally, we experimentally demonstrated that the ABL can oppose, and even reverse, the natural non-reciprocity induced by the airflow at sufficiently low Mach numbers. This result is unprecedented in the vast literature of non-reciprocal devices [15].

6. Conclusions

This paper demonstrates the potentials of the Advection Boundary Law operator synthesized on the upper boundary of a waveguide with subsonic mean-flow, in terms of both noise isolation and non-reciprocal propagation, in the plane wave regime. This study starts with the analytical evaluation of the Advection Boundary Law performances in open-field (Section 2), which provides important guidelines for the acoustical passivity limits of such special boundary operator. Then, we provide the duct-mode dispersion solutions in a 2D infinite waveguide (Section 3), and the scattering simulations of the corresponding 2D lined segment (Section 4). The scattering performances are highly correlated with the dispersion solutions. Both types of simulations illustrate the similarity between the effect of a mean-flow in the waveguide, and the ABL influence on the least attenuated duct-modes and, therefore, on the scattering performances in the plane wave regime. Introducing a synthetic boundary advection against the direction of incoming noise, allows to improve the noise isolation in that direction, also in presence of mean-flow. Such simulations have allowed to gain sufficient confidence for the experimental implementation of Section 5, in the CAIMAN wind-tunnel, available in the Laboratory of Fluid Mechanics and Acoustics of the Ecole Centrale de Lyon. We have resumed the control strategy employed to synthesize the Advection Boundary Law on the Electroacoustic Liner, which is covered by a frontal wiremesh in order to protect it from the flow. After having evaluated the effect of such wiremesh in the measured scattering coefficients, we have provided the scattering performances of the Advection Boundary Law confronted with mean-flows of Mach 0.15 and 0.3. In both cases, the synthetic boundary advection allows to improve the isolation in the direction opposite to the artificial boundary advection speed. Nevertheless, increasing the flow speed weakens the downstream isolation performances. Moreover, the presence of the frontal wiremesh entails an optimal value of the synthetic boundary advection speed. As non-reciprocal propagation is concerned, the Advection Boundary Law has demonstrated to be able to counteract the natural non-reciprocal effect induced by the flow. Nevertheless, as Mach reaches 0.3, the non-reciprocity induced by the Advection Boundary Law targeting higher isolation in the downstream direction, is significantly reduced. However, for sufficiently low Mach numbers (such as 0.15), the Advection Boundary Law has demonstrated to be able to reverse the natural non-reciprocal propagation induced by the mean-flow. A device which does not exploit mean-flow to favour its non-reciprocal isolation performances, has never been conceived before, to the best of the authors' knowledge, and represent a unique achievement of the Advection Boundary Law. Finally, in Appendix C, a 3D model of the waveguide is provided, including the wiremesh, which could be exploited for future optimization studies. The next step of this research will concern the Advection Boundary Law confronting with complex multi-modal sound fields, which are more representative of those actually excited in turbofan engines.

CRediT authorship contribution statement

E. De Bono: Writing – review & editing, Writing – original draft, Visualization, Validation, Supervision, Software, Resources, Project administration, Methodology, Investigation, Funding acquisition, Formal analysis, Data curation, Conceptualization. **M. Collet:** Supervision, Resources, Project administration, Methodology, Funding acquisition. **M. Ouisse:** Supervision, Software, Project administration, Funding acquisition. **E. Salze:** Software, Project administration. **M. Volery:** Resources. **H. Lissek:** Resources, Project administration, Funding acquisition. **J. Mardjono:** Project administration, Funding acquisition.

Declaration of competing interest

The authors declare the following financial interests/personal relationships which may be considered as potential competing interests: Emanuele De Bono reports financial support was provided by Horizon Europe. If there are other authors, they declare that they have no known competing financial interests or personal relationships that could have appeared to influence the work reported in this paper.

Acknowledgements

The SALUTE project has received funding from the Clean Sky 2 Joint Undertaking under the European Union's Horizon 2020 research and innovation programme under grant agreement N∘ 821093. This publication reflects only the author's view and the JU is not responsible for any use that may be made of the information it contains. Authors are also particularly grateful to Marie-Annick Galland and Emanuele Sarpero for their help in setting up the experimental test-bench.

Appendix A. Duct modes problem formulation

Consider a 2D infinite duct of constant cross-section h along y (as in Fig. 3) with treated boundary at $y = 0$ of normal $\mathbf{n} \equiv \hat{\mathbf{y}}$, with $\hat{\mathbf{y}}$ the unit vector along y. Assuming a time-harmonic sound field in the usual complex notation ($+\mathrm{j}\omega t$) in the duct, the convected wave equation reduces to the convected Helmholtz equation:

$$\nabla^2 \bar{p} = (\mathrm{j}k_0 + M_\infty \partial_x)^2 \bar{p}. \tag{A.1}$$

Such sound field must also satisfy the ABL on $y = 0$, given by Eq. (8). The solution to this problem can be written as:

$$\bar{p}(t, \omega, x, y) = e^{\mathrm{j}\omega t} \sum_{m=0}^{\infty} A_m \psi_m(\omega, y) e^{-\mathrm{j}k_{x,m}(\omega) x}, \tag{A.2}$$

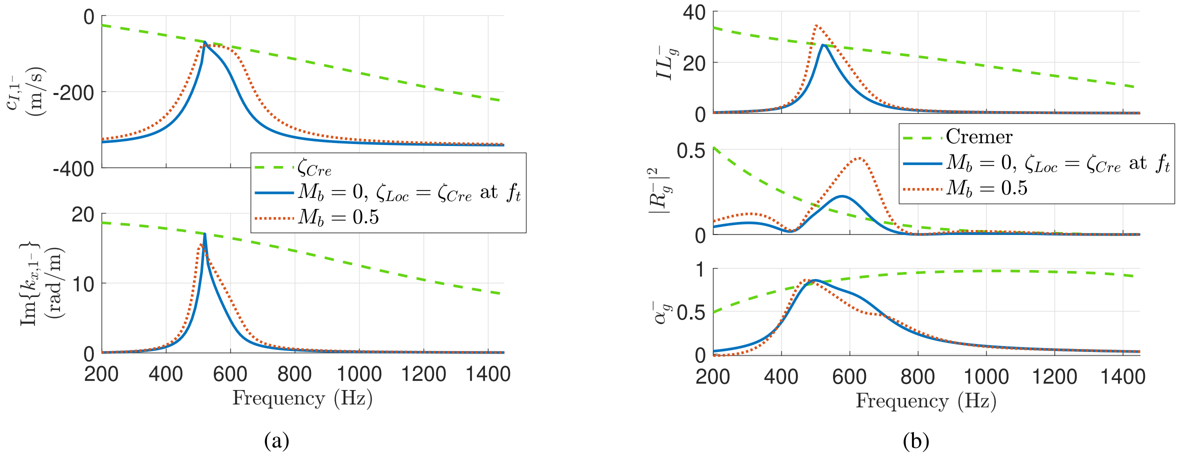

Fig. B.1. Comparison between the ABL and the Cremer impedance both in terms of dispersion solutions (a), and scattering coefficients (b), in a 2D waveguide.

where $\psi_m(y)$, the so-called *duct modes*, solutions of the eigenvalue problem:

$$\partial_y^2 \psi_m(\omega, y) = \left(-k_0^2 + 2M_\infty k_0 k_{x,m} + (1 - M_\infty^2)\right)\psi_m(\omega, y) \quad \text{for y} \in [0, h] \tag{A.3a}$$

$$\partial_y \psi_m(\omega, y) = -\mathrm{j}k_0 \eta_{\mathrm{Loc}} \left[1 - (M_b + 2M_\infty)\frac{k_{x,m}}{k_0} + (M_\infty^2 + 2M_\infty M_b)\left(\frac{k_{x,m}}{k_0}\right)^2 - M_\infty^2 M_b \left(\frac{k_{x,m}}{k_0}\right)^3\right]\psi_m(\omega, y) \quad \text{for } y = 0, \tag{A.3b}$$

where the eigenfunctions are the duct-mode shapes $\psi_m(\omega, y)$ and the eigenvalues are the wavenumbers $k_{x,m}$. Observe that Eq. (A.3a) is obtained by replacing Eq. (A.2) in Eq. (A.1), while Eq. (A.3b) is obtained by replacing Eq. (A.2) in Eq. (8). Notice that, for $M_\infty = 0$, we retrieve the eigenvalue problem of duct modes in absence of mean flow, reported in [12]. Observe also that a mean-flow $M_\infty \neq 0$, or an ABL with $M_b \neq 0$, brings about the presence of the eigenvalue $k_{x,m}$ also in the BC. Solutions for such eigenvalue problem can be found by Finite Elements (FEs), where the BC of Eq. (A.3b) is assimilated in the weak formulation of Eqs. (A.3), in an analogous way as reported in Appendix A of [12].

Appendix B. Comparison with Cremer impedance

In this Appendix, the ABL is compared to a local SDOF impedance tuned on the Cremer one [2,3] at a target frequency. The tuning of the local SDOF impedance is obtained by imposing the ζ_{Loc} of Eq. (22), equal to the Cremer normalized impedance:

$$\zeta_{\mathrm{cre}}(\omega) = (a_{\mathrm{cre}} - \mathrm{j}b_{\mathrm{cre}})\frac{k_0 h}{\pi}, \tag{B.1}$$

with $a_{\mathrm{cre}} = 0.929$ and $b_{\mathrm{cre}} = 0.744$, from [5]. Hence, by imposing $\zeta_{\mathrm{Loc}} = \zeta_{\mathrm{cre}}$ at a target frequency $f_t = 520$ Hz, we obtain the following parameters for ζ_{Loc}:

$$f_d = f_t \sqrt{1 + \frac{\rho_0 b_{\mathrm{cre}} h}{\pi \mu_M M_0}} \tag{B.2a}$$

$$r_d = a_{\mathrm{cre}} \frac{2 f_t h}{c_0}. \tag{B.2b}$$

Hence, for any choice of μ_M, it is possible to find the f_d (and hence the μ_K from $f_d = f_0\sqrt{\mu_K/\mu_M}$) and r_d from Eqs. (B.2) and (B.2b), such that $\zeta_{\mathrm{Loc}} = \zeta_{\mathrm{cre}}$ at f_t.

Remind that the normalized Cremer impedance ζ_{Loc} of Eq. (B.1), if applied on one side of a 2D infinite waveguide, provides the coalescence of $k_{x,1}$ and $k_{x,2}$ [2,3], with the duct modes numbered from the least attenuated one (which is mode 1) in ascending order, as done in Section 3. This means that ζ_{Cre} provides the highest attenuation of mode 1, i.e. the maximum value of $|\mathrm{Im}\{k_{x,1}\}|$, assuring the highest transmission loss in an infinite waveguide.

In Fig. B.1, we compare the performances of the ζ_{cre}, with the ζ_{Loc} tuned on ζ_{cre} at f_t, and with the ABL with a $M_b = 0.5$ and $r_d = 0.25$. Fig. B.1(a) compares the three impedances in terms of dispersion solutions of mode 1^- (employing the same indicators as in Section 3), while Fig. B.1(b) shows the corresponding scattering coefficients. Notice that ζ_{cre} provides the highest $|\mathrm{Im}\{k_{x,1^-}\}|$ at all frequencies, reached by ζ_{Loc} at $f_t = 520$ Hz. Nevertheless, the ABL is capable to improve the IL_g^- at f_t and enlarge the bandwidth of highest isolation, thanks to a significant increase of the backward reflection $|R_g^-|^2$. Indeed, in a duct with finite dimension, the mode-merging design method fails to provide the highest TL_g [52], due to the effect of backward reflection. A detailed discussion about the optimality of the Cremer impedance and its relationship with real operators (such as SDOF resonators or the ABL itself) is out of the scope of the present paper. Nevertheless, Fig. B.1 provides an opening about this topic.

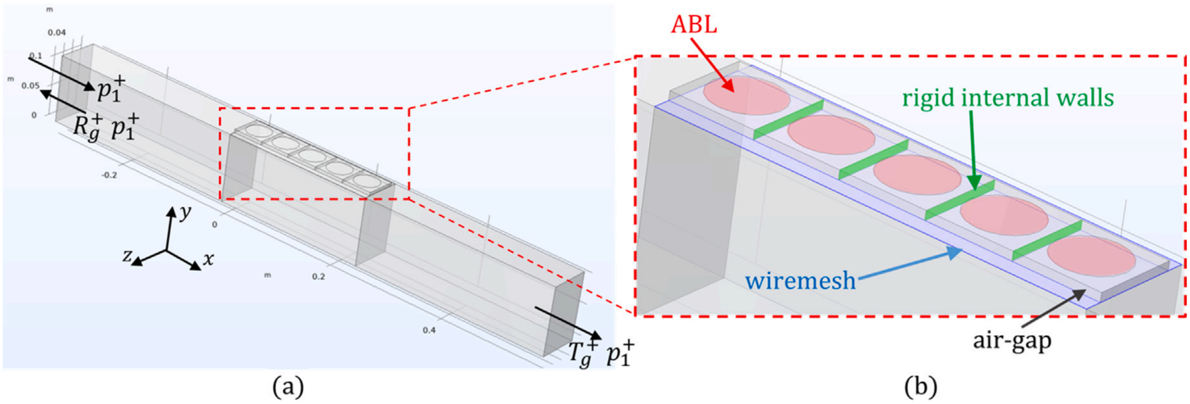

Fig. C.1. 3D model for scattering simulations.

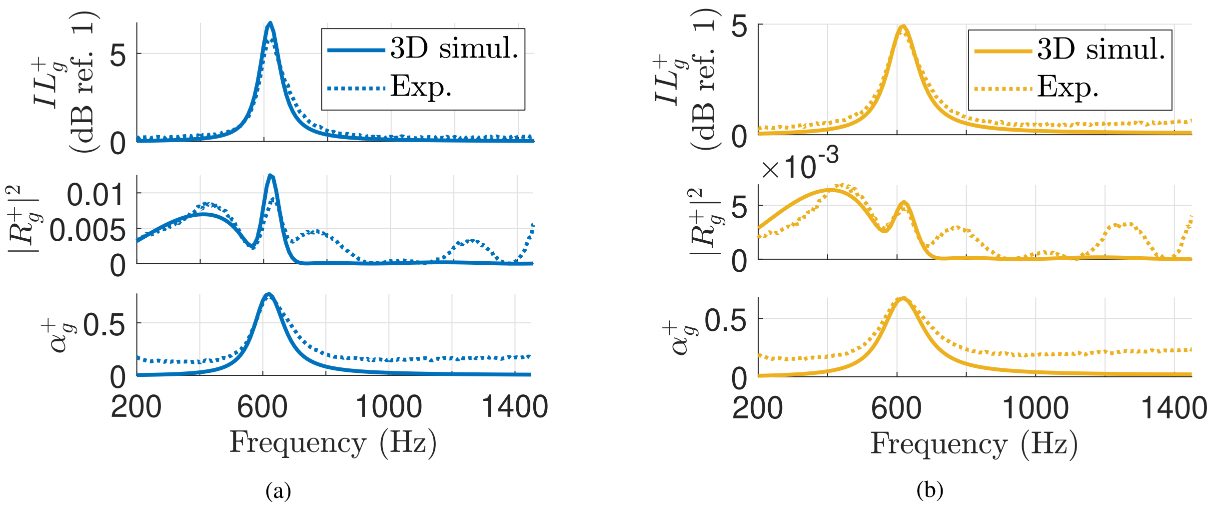

Fig. C.2. Comparison between the 3D simulations and the experimental results, in case of $M_\infty = 0$, with ABL parameters $r_d = 1$, $\mu_M = 0.5$, $f_d = f_0$, without wiremesh (a) and with wiremesh (b).

Appendix C. Scattering simulations in 3D waveguide

In this section, we provide a 3D numerical model which is more representative of the actual lined segment applied in the CAIMAN test-rig. Fig. C.1a shows the 3D waveguide geometry along with the definition of the first column of the scattering matrix of Eq. (23). Fig. C.1b zooms on the lined segment. Notice that the ABL is applied on the circles representing the ERs' speakers, by imposing the normal displacement given by Eq. (7). Each ER cell is separated by rigid internal walls, and is facing an air-gap of about 5 mm between the ERs' speakers and the wiremesh. The inviscid and irrotational mean-flow along x is defined in the entire waveguide, except in the domain representing the wiremesh and the adjacent air-gaps. This approximation serves to simulate the separation, the wiremesh is supposed to achieve, between the convected air-domain from the one facing the EL. A *vortex sheet* internal BC is applied at the interface of the wiremesh with the convected air domain, assuring the continuity of the normal stress (the pressure) and the normal displacement, while allowing for a jump in the tangential component of the total velocity. The wiremesh domain is modelled by defining the effective sound speed and density from the Johnson–Champoux–Allard (JCA) model [46] based upon the parameters listed in Table 2. Observe that the perforated plate supporting the wiremesh has large perforations which allow, at a first stage, to consider the plate as acoustically transparent.

The scattering problem is solved in frequency domain by FEs in COMSOL. Figs. C.2 to C.4 show the comparison of the scattering coefficients obtained by the 3D simulations and by experimental measurements in the actual CAIMAN test-rig. In particular, we validate the 3D numerical model against the effect of wiremesh (Fig. C.2), the effect of M_∞ (Fig. C.3) and the effect of M_b (Fig. C.4). Fig. C.2 compares the 3D simulations with the experiments for $M_\infty = 0$, with ABL parameters $r_d = 1$, $\mu_M = 0.5$, $f_d = f_0$, in case of no wiremesh (Fig. C.2a) and with wiremesh (Fig. C.2b). Notice that the shape of the Insertion Losses is well captured by the 3D model, especially around resonance. The experimental absorption coefficients deviate from the numerical ones below and after resonance. This is so, because of the natural dissipation present in the physical system. The experimental reflection

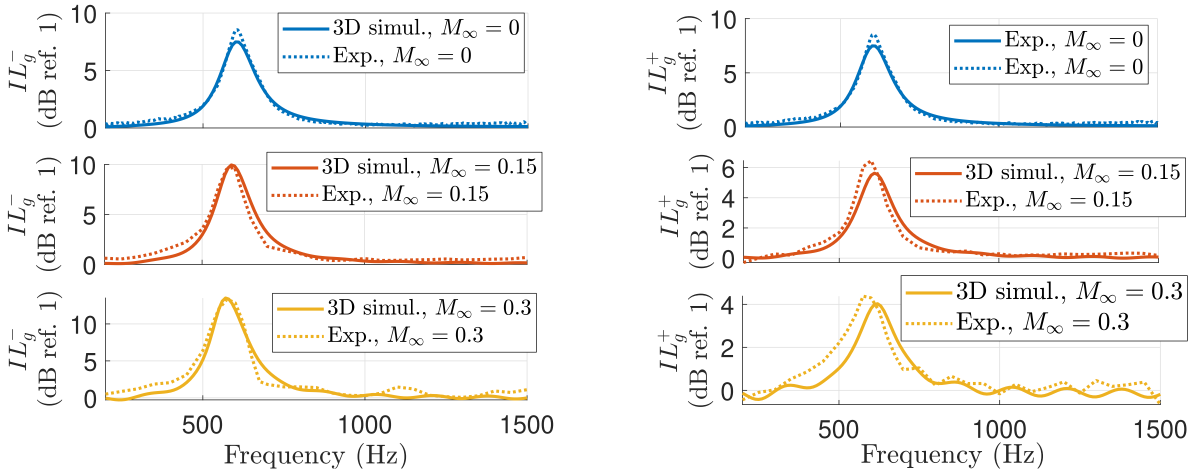

(a) (b)

Fig. C.3. Experimental Insertion Losses, in case of varying M_∞, with ABL parameters $r_d = 0.25$, $\mu_M = 0.5$, $f_d = f_0$, and $M_b = 0$.

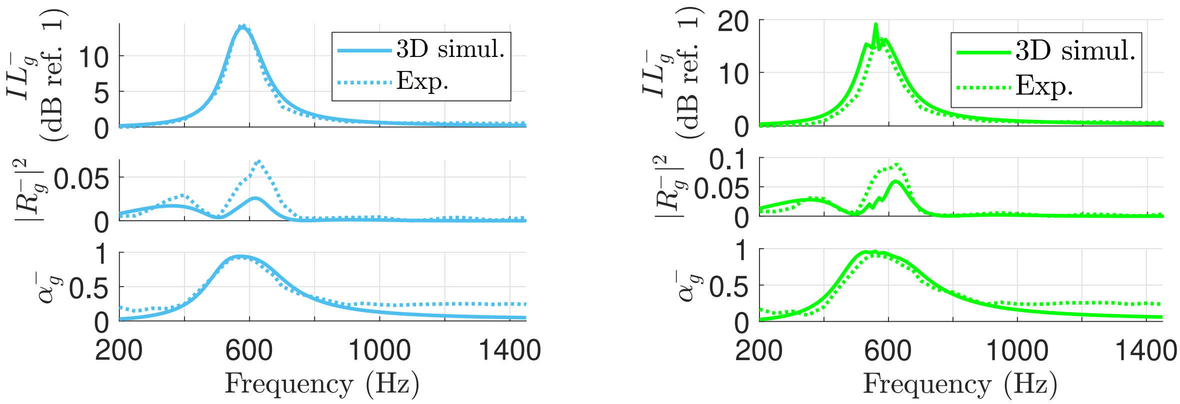

(a) (b)

Fig. C.4. Comparison between experiments and 3D simulations, in terms of the coefficients of the second column of the scattering matrix of Eq. (23), in case of $M_\infty = 0.15$, with ABL parameters $r_d = 0.25$, $\mu_M = 0.5$, $f_d = f_0$, and $M_b = 1$ (a) or $M_b = 2$ (b).

coefficients' spectra feature additional oscillations in frequency compared to the numerical ones. However, considering the scale of the power reflection coefficient, these errors do not significantly impact the isolation levels. Fig. C.3 shows the comparison between 3D simulations and measurements in case of ABL with $M_b = 0$, $r_d = 0.25$, $\mu_M = 0.5$, $f_d = f_0$ and varying M_∞. The increase of IL_g^- with M_∞ is very well captured. Some discrepancy, instead, can be noticed on the IL_g^+ plots, especially in case of $M_\infty = 0.3$. At higher M_∞, the IL_g^+ is reduced, therefore even errors below 1 dB become more evident. Nevertheless, we should keep in mind the large simplifications involved in the modelling of both the air-domain (inviscid and irrotational fluid) and the ERs. Moreover, the experimental campaign was conducted in different days, which presented different environmental conditions (such as temperature and humidity) which significantly impact the mechanical properties of the ERs' speakers [53]. This adds up to the inevitable model uncertainties, such as also time-delay [36] of the digital controller. However, it is interesting to notice that, for $M_\infty = 0.3$, the 3D simulations are able to capture also the oscillations of IL_g^+ in the high frequencies. Finally, in Fig. C.4 the comparison between 3D simulations and experiments is reported in case of $M_\infty = 0.15$ and ABL with $M_b = 1$ (Fig. C.4a) and $M_b = 2$ (Fig. C.4b). As in Fig. C.2, the largest percentage errors appear in the reflection coefficients, especially close to f_d, despite the general trends of measurements are satisfactorily captured by simulations. Once again, the small absolute errors in $|R_g^-|^2$ do not impact significantly the isolation levels.

This 3D model might be exploited in future studies, by including the wiremesh effect for the optimization of the boundary operator synthesized on the EL.

Data availability

The data that has been used is confidential.

References

[1] C. Bardos, G. Lebeau, J. Rauch, Sharp sufficient conditions for the observation, control, and stabilization of waves from the boundary, SIAM J. Control Optim. 30 (1992) 1024–1065.

[2] L. Cremer, Theory regarding the attenuation of sound transmitted by air in a rectangular duct with an absorbing wall, and the maximum attenuation constant produced during this process, Acustica 3 (1953) 249.

[3] B. Tester, The optimization of modal sound attenuation in ducts, in the absence of mean flow, J. Sound Vib. 27 (1973) 477–513, http://dx.doi.org/10.1016/S0022-460X(73)80358-X, URL: https://linkinghub.elsevier.com/retrieve/pii/S0022460X7380358X.

[4] A.M.N. Spillere, J.A. Cordioli, Optimum acoustic impedance in circular ducts with inviscid sheared flow: Application to turbofan engine intake, J. Sound Vib. 443 (2019) 502–519.

[5] S.W. Rienstra, Fundamentals of Duct Acoustics, Von Karman Institute Lecture Notes, 2015.

[6] A.W. Guess, Calculation of perforated plate liner parameters from specified acoustic resistance and reactance, J. Sound Vib. 40 (1975) 119–137.

[7] B. Betgen, Comportement d'un Absorbant Actif en Écoulement: Étude Théorique et Expérimentale (Ph.D. thesis), 2010.

[8] Y. Renou, Y. Aurégan, Failure of the Ingard–Myers boundary condition for a lined duct: An experimental investigation, J. Acoust. Soc. Am. 130 (2011) 52–60.

[9] H.F. Olson, E.G. May, Electronic sound absorber, J. Acoust. Soc. Am. 25 (1953) 1130–1136, http://dx.doi.org/10.1121/1.1907249, URL: http://asa.scitation.org/doi/10.1121/1.1907249.

[10] M. Collet, P. David, M. Berthillier, Active acoustical impedance using distributed electrodynamical transducers, J. Acoust. Soc. Am. 125 (2009) 882–894.

[11] S. Karkar, E. De Bono, M. Collet, G. Matten, M. Ouisse, E. Rivet, Broadband nonreciprocal acoustic propagation using programmable boundary conditions: From analytical modeling to experimental implementation, Phys. Rev. Appl. 12 (2019) 054033, http://dx.doi.org/10.1103/PhysRevApplied.12.054033, URL: https://link.aps.org/doi/10.1103/PhysRevApplied.12.054033. arXiv:1906.09099.

[12] E. De Bono, M. Collet, M. Ouisse, The advection boundary law in absence of mean flow: Passivity, nonreciprocity and enhanced noise transmission attenuation, J. Sound Vib. (2024) 118603, http://dx.doi.org/10.1016/j.jsv.2024.118603, URL: https://www.sciencedirect.com/science/article/pii/S0022460X24003663.

[13] G. Montseny, Diffusive representation of pseudo-differential time-operators, 1998.

[14] A.A. Oberai, M. Malhotra, P.M. Pinsky, On the implementation of the Dirichlet-to-Neumann radiation condition for iterative solution of the Helmholtz equation, Appl. Numer. Math. 27 (1998) 443–464.

[15] R. Fleury, D. Sounas, M.R. Haberman, A. Alu, Nonreciprocal acoustics, Acoust. Today 11 (2015) 14–21.

[16] S. Devasia, Should model-based inverse inputs be used as feedforward under plant uncertainty? IEEE Trans. Autom. Control 47 (2002) 1865–1871.

[17] E. De Bono, M. Morell, M. Collet, E. Gourdon, A. Ture Savadkoohi, M. Ouisse, C.H. Lamarque, Model-inversion control to enforce tunable duffing-like acoustical response on an electroacoustic resonator at low excitation levels, J. Sound Vib. 570 (2024) http://dx.doi.org/10.1016/j.jsv.2023.118070.

[18] C.E. da Silveira Zanin, A. Labetoulle, E. De Bono, E. Gourdon, M. Collet, A. Ture Savadkoohi, Experimental evidences of nonlinear programmable electroacoustic loudspeaker, Build. Acoust. 30 (2023) 249–263, http://dx.doi.org/10.1177/1351010X231184040.

[19] M. Morell, E. Gourdon, M. Collet, A. Ture Savadkoohi, E. De Bono, C.-H. Lamarque, Towards digitally programmed nonlinear electroacoustic resonators for low amplitude sound pressure levels: Modeling and experiments, J. Sound Vib. 584 (2024) 118437, http://dx.doi.org/10.1016/j.jsv.2024.118437, URL: https://www.sciencedirect.com/science/article/pii/S0022460X24002001.

[20] M. Morell, M. Collet, E. Gourdon, A.T. Savadkoohi, E. De Bono, Experimental validation of the analytical modelling of a digitally created duffing acoustic nonlinear oscillator at low amplitudes, Mech. Ind. 26 (2025) 2.

[21] M. Morell, E. Gourdon, M. Collet, A. Ture Savadkoohi, E. De Bono, Nonlinear digitally created electroacoustic absorber designed for acoustic energy pumping, 2024, pp. 4807–4810, http://dx.doi.org/10.61782/fa.2023.0862.

[22] E. Rivet, S. Karkar, H. Lissek, Broadband low-frequency electroacoustic absorbers through hybrid sensor-/shunt-based impedance control, IEEE Trans. Control Syst. Technol. 25 (2017) 63–72, http://dx.doi.org/10.1109/TCST.2016.2547981, URL: http://ieeexplore.ieee.org/document/7453162/.

[23] E. De Bono, D. Ponticelli, S. De Rosa, G. Petrone, M. Ouisse, E. Sadoulet-Reboul, R. Teloli, Active impedance control optimization for attenuation of acoustic cavity modes, in: 30th AIAA/CEAS Aeroacoustics Conference (2024), 2024, p. 3195.

[24] R. Boulandet, H. Lissek, S. Karkar, M. Collet, G. Matten, M. Ouisse, M. Versaevel, Duct modes damping through an adjustable electroacoustic liner under grazing incidence, J. Sound Vib. 426 (2018) 19–33, http://dx.doi.org/10.1016/j.jsv.2018.04.009, URL: https://linkinghub.elsevier.com/retrieve/pii/S0022460X18302281.

[25] E.D. Bono, M. Collet, S. Karkar, G. Matten, M. Ouisse, Non-local boundary control for broadband non-reciprocal propagation : Analytical demonstration and experimental validation, in: Euro-Mediterranean Conference on Structural Dynamics and Vibroacoustics, 2020, pp. 17–20.

[26] K. Billon, E. De Bono, M. Perez, E. Salze, G. Matten, M. Gillet, M. Ouisse, M. Volery, H. Lissek, J. Mardjono, M. Collet, In flow acoustic characterisation of a 2D active liner with local and non local strategies, Appl. Acoust. 191 (2022) 108655, http://dx.doi.org/10.1016/j.apacoust.2022.108655.

[27] K. Billon, E. De Bono, M. Perez, E. Salze, G. Matten, M. Gillet, M. Ouisse, M. Volery, H. Lissek, J. Mardjono, M. Collet, Experimental assessment of an active (acoustic) liner prototype in an acoustic flow duct facility, in: Health Monitoring of Structural and Biological Systems XV, Vol. 11593, International Society for Optics and Photonics, 2021, p. 84, http://dx.doi.org/10.1117/12.2583099.

[28] K. Billon, M. Collet, E. Salze, M. Gillet, M. Ouisse, M. Volery, H. Lissek, J. Mardjono, 2D active liner experimental results in acoustic flow duct facility, in: Smart Materials, Adaptive Structures and Intelligent Systems, Vol. 86274, American Society of Mechanical Engineers, 2022, V001T03A001.

[29] K. Billon, M. Gillet, E. Salze, M. Volery, E. De Bono, M. Ouisse, H. Lissek, M. Collet, J. Mardjono, Smart acoustic lining for UHBR technologies engine: from the design of an electroacoustic metasurface to experimental characterization under flow, in: Active and Passive Smart Structures and Integrated Systems XVII, Vol. 12483, SPIE, 2023, p. 72, http://dx.doi.org/10.1117/12.2658519.

[30] E. De Bono, M. Collet, M. Ouisse, Breaking the limitations of local impedance noise control: passivity, and scattering performances of the advection boundary law, in: Active and Passive Smart Structures and Integrated Systems XVIII, Vol. 12946, SPIE, 2024, pp. 302–311.

[31] E. De Bono, M. Collet, M. Ouisse, E. Salze, M. Volery, H. Lissek, J. Mardjono, The advection boundary law in presence of mean-flow and spinning modes, in: Active and Passive Smart Structures and Integrated Systems XVIII, Vol. 12946, SPIE, 2024, pp. 312–319.

[32] E. De Bono, M. Collet, K. Billon, E. Salze, H. Lissek, M. Volery, M. Ouisse, J. Marjono, Smart acoustic lining for UHBR technologies engine part 1: Design of an electroacoustic liner and experimental characterization under flow in rectangular cross-section ducts, in: 30th AIAA/CEAS Aeroacoustics Conference (2024), 2024, p. 3303.

[33] E. de Bono, M. Ouisse, M. Collet, E. Salze, H. Lissek, M. Volery, J. Mardjono, Programmable electroacoustic boundaries in acoustic waveguides: enhanced attenuation and non-reciprocal sound propagation, in: 10th ECCOMAS Thematic Conference on Smart Structures and Materials, 2023.

[34] E. De Bono, M. Collet, K. Billon, E. Salze, H. Lissek, M. Volery, M. Ouisse, J. Marjono, Smart acoustic lining for UHBR technologies engine part 2: Acoustic treatment at the intake of a scaled turbofan nacelle, in: 30th AIAA/CEAS Aeroacoustics Conference (2024), 2024, p. 3304.
[35] E. De Bono, M. Ouisse, M. Collet, E. Salze, J. Mardjono, A nonlocal boundary control, from plane waves to spinning modes control, in: Active and Passive Smart Structures and Integrated Systems XVII, Vol. 12483, SPIE, 2023, p. 74, http://dx.doi.org/10.1117/12.2658382.
[36] E. De Bono, M. Collet, G. Matten, S. Karkar, H. Lissek, M. Ouisse, K. Billon, T. Laurence, M. Volery, Effect of time delay on the impedance control of a pressure-based, current-driven electroacoustic absorber, J. Sound Vib. 537 (2022) 117201, http://dx.doi.org/10.1016/j.jsv.2022.117201.
[37] R. Fleury, D.L. Sounas, C.F. Sieck, M.R. Haberman, A. Alù, Sound isolation and giant linear nonreciprocity in a compact acoustic circulator, Science 343 (2014) 516–519, http://dx.doi.org/10.1126/science.1246957.
[38] Y. Aurégan, V. Achilleos, V. Pagneux, Use flow to achieve an unidirectional acoustic propagation in a duct, in: EForum Acusticum 2020, 2020, pp. 773–775.
[39] U. Ingard, Influence of fluid motion past a plane boundary on sound reflection, absorption, and transmission, J. Acoust. Soc. Am. 31 (1959) 1035–1036.
[40] M.K. Myers, On the acoustic boundary condition in the presence of flow, J. Sound Vib. 71 (1980) 429–434.
[41] M.K. Myers, An exact energy corollary for homentropic flow, J. Sound Vib. 109 (1986) 277–284.
[42] F. Mainardi, Energy velocity for hyperbolic dispersive waves, Wave Motion 9 (1987) 201–208.
[43] U. Ingard, Noise Reduction Analysis, Jones & Bartlett Publishers, 2009.
[44] E. Sarpero, D. Dragna, E. Gourdon, M.-A. Galland, Nonlinear broadband time-domain admittance boundary condition applied to a flow duct with perforated liner, 2023.
[45] A. International, ASTM E2611-09 Standard Test Method for Measurement of Normal Incidence Sound Transmission of Acoustical Materials Based on the Transfer Matrix Method, ASTM, 2009.
[46] J.F. Allard, N. Atalla, Propagation of Sound in Porous Media: Modelling Sound Absorbing Materials, John Wiley & Sons, 2009.
[47] L.L. Beranek, T. Mellow, Acoustics: Sound Fields and Transducers, Academic Press, Oxford OX5 1GB, UK, 2012, http://dx.doi.org/10.1016/C2011-0-05897-0.
[48] E. De Bono, M. Collet, S. Karkar, G. Matten, H. Lissek, T. Laurence, Electroacoustic resonators: System identification and stability, in: Proceedings of the 26th International Congress on Sound and Vibration, ICSV 2019, CONF, Canadian Acoustical Association, 2018.
[49] R.A. Pease, A comprehensive study of the howland current pump a comprehensive study of the howland current pump applications for the howland current pump AN-1515, Most 29 (2008) 12, URL: http://www.national.com/an/AN/AN-1515.pdf.
[50] J. Steele, T. Green, Tame those versatile current source circuits, Electron. Des. 61 (1992).
[51] M.L. Munjal, A.G. Doige, Theory of a two source-location method for direct experimental evaluation of the four-pole parameters of an aeroacoustic element, J. Sound Vib. 141 (1990) 323–333.
[52] J. Zhang, W. Shu, R. Yan, L. Du, X. Sun, Optimum acoustic impedance for a finite-length nacelle liner of turbofan engine, in: AIAA AVIATION 2023 Forum, 2023, p. 3738.
[53] A. Novak, Modeling viscoelastic properties of loudspeaker suspensions using fractional derivatives, J. Audio Eng. Soc. 64 (2016) 35–44.